Journal Pre-proofs

Exploring the use of cheap natural raw materials to reduce the internal concentration polarization in thin-film composite forward osmosis membranes

Abolfazl Arjmandi, Majid Peyravi, Mehrzad Arjmandi, Ali Altaee

PII: S1385-8947(20)31611-9
DOI: https://doi.org/10.1016/j.cej.2020.125483
Reference: CEJ 125483

To appear in: *Chemical Engineering Journal*

Received Date: 5 April 2020
Revised Date: 9 May 2020
Accepted Date: 12 May 2020

Please cite this article as: A. Arjmandi, M. Peyravi, M. Arjmandi, A. Altaee, Exploring the use of cheap natural raw materials to reduce the internal concentration polarization in thin-film composite forward osmosis membranes, *Chemical Engineering Journal* (2020), doi: https://doi.org/10.1016/j.cej.2020.125483

Exploring the use of cheap natural raw materials to reduce the internal concentration polarization in thin-film composite forward osmosis membranes

Abolfazl Arjmandi[a], Majid Peyravi[a*], Mehrzad Arjmandi[b], Ali Altaee[c]

[a]Department of Chemical Engineering, Babol Noshirvani University of Technology, Shariati Av., Babol, Iran.

[b]Chemical Engineering Department, Faculty of Engineering, Ferdowsi University of Mashhad, Mashhad, Iran

[c]Centre for Technologies for Water and Wastewater, School of Civil and Environmental Engineering, University of Technology Sydney, Australia

[*]Corresponding author:
Majid Peyravi
Department of Chemical Engineering, Babol Noshirvani University of Technology, Shariati Av., Babol, Iran.
P.O. Box: 484, Postal Code: 47148-71167.
Tel/Fax: +98 1132320342
Email: majidpeyravi@nit.ac.ir, majidpeyravi@gmail.com

Graphical Abstract

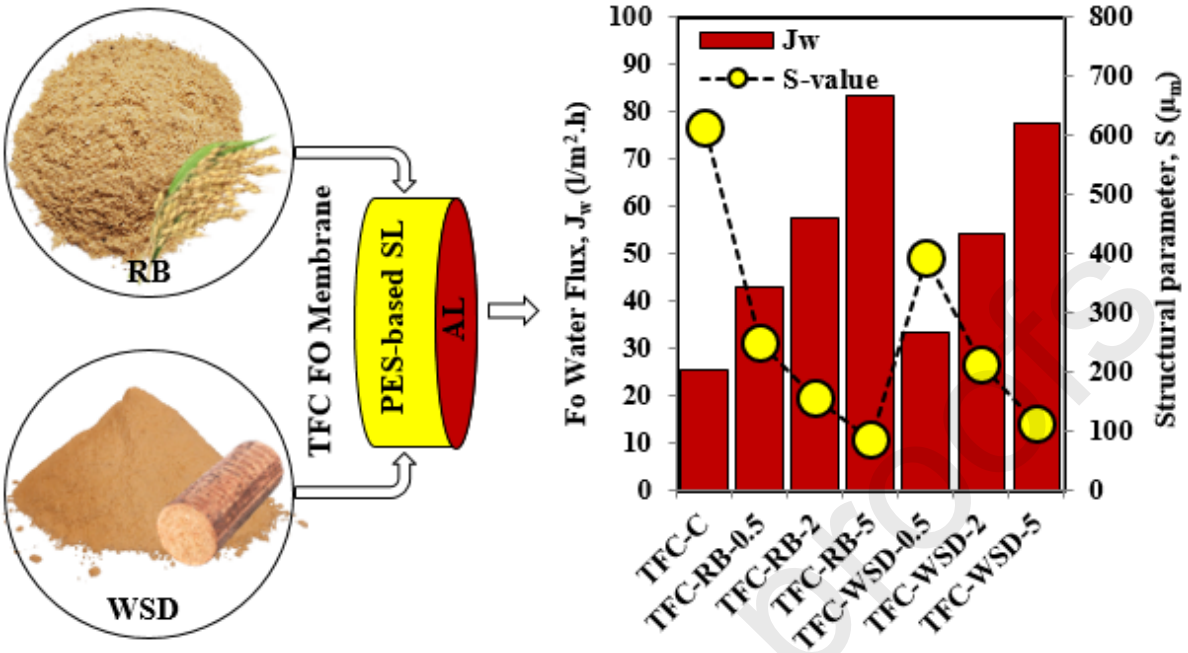

Abstract

Internal concentration polarization (ICP) is a significant problem in Forward osmosis (FO) membranes, which reduces the water flux. In order to mitigate the ICP phenomenon, rice bran (RB) and wood sawdust (WSD) particles were selected as natural green pore formers and incorporated into the polyethersulfone (PES) matrix to fabricate mixed matrix membranes (MMMs). Fabricated MMMs were used as the porous support layer (SL) to make thin-film composite (TFC) FO membranes. Firstly, the water uptake experiment was performed to evaluate the water adsorption capacity of the RB and WSD particles. Furthermore, all samples were characterized by FTIR, FESEM, AFM, XPS, DLS, static contact angle (CA), and tensile strength. Also, performance tests in reverse osmosis (RO) and the FO units were performed to evaluate the fabricated membranes. The results showed that the use of RB and WSD particles dramatically reduced the structural parameter in all MMMs, resulting in lower ICP effects and high water flux. Due to the softer structure, smaller size, and more water uptake, the RB-based TFC membranes recorded better results. The TFC-RB-5 (with 5% of RB in the SL) was the best membrane with a water flux of about 65.71 L/m^2.h for Caspian seawater desalination, while the FO water flux for DI water as the feed solution (FS) was 83.65 L/m^2.h. The present study showed the membranes made in this study are competitive with the existing FO membranes and very cost-effective for broad applications.

Keyword: Forward osmosis, desalination, internal concentration polarization, rice bran, wood sawdust.

1. Introduction

The scarcity of freshwater has led to extensive research to optimally use water resources, reuse of the existing industrial and domestic wastewater, as well as converting saline water resources into freshwater. Rivers, lakes, seas, and oceans, which cover about 70% of the Earth's surface, cannot be used as drinking water without treatment [1]. Thus, the use of an eco-friendly, practical and low-cost method to convert vast saline water resources into freshwater for agricultural or as drinking water will have significant economic and environmental benefits. Amongst different methods of water and wastewater treatment, membrane processes are considered as an attractive option due to their low energy consumption, low investment cost, and usability in the separation of temperature-sensitive materials [2,3]. Reverse osmosis (RO) process has been widely used for seawater desalination and separation processes [4-6]. However, due to the high energy consumption of the RO system and their high fouling tendency, efforts are made to find alternative filtration technologies to replace the RO process or reduce its energy consumption and fouling problem [7-9].

In recent years, forward osmosis (FO) has attracted a lot of attention as one of the newest and most efficient membrane processes [10-12]. In the FO process, the osmotic pressure difference between the concentration of feed solution (FS) and a high concentration draw solution (DS), across the membrane is the driving force for freshwater recovery [13]. Due to the lack of hydraulic pressure, the FO process consumes much less energy than pressure-driven membrane processes (i.e. RO) and has low fouling tendency [14,15]. Like the RO process, thin-film composite (TFC) membranes are the most common membranes used in the FO process [16-18]. TFC FO membranes consist of a thin active layer (AL) on top of a porous support layer (SL). There are two operating modes in the FO process, FO mode when the DS is against the SL of the membrane, and PRO mode when the FS is against the AL of the FO membrane. Due to less fouling tendency of FO mode, this orientation is much suitable for low-quality feeds and wastewater treatment [19,20]. The most critical problem in the TFC FO membranes is the

concentration polarization (CP), which mainly originates from the asymmetric structure of these membranes and reduces the active osmotic driving force, which in turn negatively impacts the performance of the FO membrane [21,22]. Dilutive internal concentration polarization (DICP) is the significant type of CP that occurs in the FO process, causing a sharp decline in the water flux (J_w) in the FO mode [22]. The adverse effects of DICP can be improved by modifying the physicochemical properties of the SL, such as reducing the structural parameter (S) [21,23]. The intensity of DICP can be determined by S-value, which has a direct relationship with SL thickness (t) and tortuosity (τ), and has an inverse relationship with the SL porosity (ε) ($S = t\tau/\varepsilon$) [23]. One achievable and practical method to decrease the S-value is to use various functional fillers and pore formers in the SL structure [24-26]. In recent years, some of water-stable and water-unstable Metal-organic frameworks (MOFs), as attractive nanoparticles (NPs), have been used to decrease the S-value of osmotically driven membrane processes [25-29]. However, the use of synthetic NPs, although yielding excellent results, is usually achieved at a high cost that is an essential obstacle to commercialization. Therefore, finding materials that in addition to reducing the S-value, are also inexpensive, is a significant step towards commercializing TFC FO membranes.

Annually, million tons of wood sawdust (WSD) and rice bran (RB) as by-products of the wood and agricultural industry is not appropriately used and dumped or burned, which in turn causes significant environmental damages [30,31]. One of the most recent applications of these low cost and easy access by-products, directly or in combination with other materials, is to use them as surface adsorbents in removing contaminants from industrial and non-industrial effluents. Yet, different forms of these materials have been used to adsorb dyes [32-36], heavy metals [33,35,37-43], organic compounds [33,35], ions [33,35,39-44]. Because of porous structure and water resistance, WSD and RB are exciting options to modify the SL structure of the TFC membranes. According to our investigation, RB has not been used in several membrane

technologies to alter the structure. But WSD was used in limited cases as filler and pore former in membranes. The impact of WSD as pore former in the SL structure of the ceramic tubular membrane has been studied [45,46]. Studies found that with increasing temperature and degradation of WSD particles in the SL structure as well as increasing the percentage of WSD used in the primary polymeric solution, the number of pores and consequently SL porosity was increased.

Furthermore, previous literature evaluated the impact of using partially modified WSD particles in the polymeric membrane [47]. Accordingly, the surface energy and surface hydrophilicity of the WSD-containing membrane has been increased. Recently, the application of WSD as a filler to increase the porosity of SL in the TFC RO membrane was studied [48]. The effect of the implementation of WSD on salt rejection, pure water flux and mechanical resistance of the TFC RO membrane in the desalination process revealed excellent salt rejection and water flux. One of the most significant results of this study is the decrease of membrane mechanical resistance due to the porosity increment, which indicates the unattractiveness of this method in pressure-driven membrane processes such as the RO process. Accordingly, it seems that this modifying method can yield better results in non-pressure-driven membrane processes (e.g. FO).

For this purpose, RB and WSD particles as porous fillers were selected as pore formers and incorporated into the polyethersulfone (PES) to prepare the mixed matrix membranes (MMMs) as SL for the TFC FO membranes. Hydrophilic PES was used in the SL of the TFC FO membranes because of its excellent chemical and mechanical properties [49]. The corresponding PES-based TFC FO membranes were synthesized via the formation of a thin polyamide (PA) layer on the MMMs by interfacial polymerization (IP) method. The water uptake test was performed to evaluate the water adsorption capacity of the RB and WSD particles. Furthermore, membrane samples were analyzed with characterization methods with

Fourier-transform infrared (FTIR), field-emission scanning electron microscopy (FESEM), atomic force microscopy (AFM), X-ray photoelectron spectroscopy (XPS), static contact angle (CA), Dynamic light scattering (DLS), tensile strength, and bulk porosity experiment to understand the physicochemical changes resulting from WSD and RB particles on the membrane characteristics. The performance of TFC membranes was evaluated in cross-flow FO and RO systems to determine water flux (J_w) and salt rejection (R) and membrane intrinsic parameters including water permeability coefficient (A), solute flux (B) and S-value. Also, the study investigated the MMM-based TFC FO membranes for the desalination of Caspian seawater. To the best of our knowledge, we believe that the results obtained from this cost-effective method are useful for the commercialization of TFC FO membranes.

2. Materials and methods

2.1. Materials and chemicals

Dimethylformamide (DMF, 99.8% purity), N-methyl-2-pyrrolidone (NMP, 99% purity), trimesoyl chloride (TMC, 98% purity), lithium chloride (LiCl, 99.9% purity), polyvinylpyrrolidone (PVP), m-phenylenediamine (MPD, 99.5% purity), n-hexane (95% purity), ethanol (99% purity), nitric acid (65% purity) and sodium chloride (NaCl, 99% purity) were supplied from Merck, Germany. Polyethersulfone (PES) (Radel®A) was purchased from Solvay Speciality Polymers, USA. Before dissolving in the NMP solvent, PES was dried at 120 °C for 10 h. All chemicals were used as received and without further purification. Deionized water (DI) with ultralow conductivity (0.9 μS/cm) was prepared in the lab. The RB and WSD particles used in this study were obtained from local rice mill and sawmill factories, respectively, in Mahmoudabad, Mazandaran, Iran. These particles were further milled and sieved several times and washed with DI water and nitric acid before use. For the desalination

process, the Caspian seawater from the northern part of Iran (Mazandaran) was used in this study (Table 1).

Table 1: Analysis of Caspian seawater at two stations.

Properties	Unit	Nour station	Gorgan station	Average
pH	---	≅ 7.10	≅ 7.10	≅ 7.10
Na	mg L^{-1}	≅ 4470	≅ 5533	≅ 5001
Ca	mg L^{-1}	≅ 160	≅ 249	≅ 204
Mg	mg L^{-1}	≅ 500	≅ 737	≅ 618
Cl	mg L^{-1}	≅ 5516	≅ 6900	≅ 6208
SO_4	mg L^{-1}	≅ 1500	≅ 2250	≅ 1875
K	mg L^{-1}	≅ 100	≅ 260	≅ 180
TDS	mg L^{-1}	≅ 12200	≅ 15900	≅ 14000

2.2. WSD and RB preparation

The RB and WSD particles were undergone some modification processes. The particles were first passed through a sieve with 25 µm mesh size (Mesh No. 500) to remove large and inappropriate particles and to provide better mechanical performance for the polymeric membrane. The sieved particles were then placed inside O-type grinding jar and milled in the Retsch planetary ball mill PM 100 bench-top unit. Milling times were identical for both samples. It is worth mentioning that the prepared particles were placed into liquid nitrogen (LN) for 3 minutes before the milling process. The milled samples were passed again through a 25 µm sieve as a final attempt to obtain more homogeneous particles. The prepared particles thoroughly washed to remove contaminants and get proper physical properties. In this step, samples were hierarchically washed by DI water, nitric acid, and DI water. Finally, the as-prepared particles were dried in a vacuum oven at 60 °C for 24 h. The dried WSD and RB particles were separately stored in sealed containers for further use.

2.3. Fabrication of MMMs

The RB and WSD particles were undergone some modification processes. Asymmetric flat sheet MMMs containing RB and WSD as filler and PES as polymeric matrix were fabricated

via a non-solvent-induced phase separation (NIPS) method [50]. Firstly, pure PES membrane was prepared by dissolving dried PES (15.5 wt%), PVP (0.5 wt%), and LiCl (3 wt%) in NMP solvent and vigorously mixed at 65 ºC for 24 h to obtain a homogeneous solution. Then, for removing all entrained bubbles, the homogenous casting solution was left immobilized for 12 hours. The final solution was then cast on a glass plate by use of a casting knife to achieve a final thickness of around 50-55 μm and immediately immersed in a coagulation water bath over 48 h to prepare the final PES membrane (labeled as PES-C). Several loadings of RB and WSD particles ranging from 0.5 to 5 wt% (based on polymer content) were added to the first polymeric solutions to compare the impact of adding particles to the PES membrane. In fact, the fabrication of MMMs was similar to that of the neat PES membrane with an additional step of adding RB and WSD particles. For each MMM, a weighted amount of particle was firstly added to NMP solvent under vigorous stirring for 2 hours at room temperature. Then, PES was added to the solution and mixed for 24 hours until the polymer is completely dissolved. Thus, taking into account the pure PES substrate, seven membranes were fabricated in total. These membranes were labeled as PES-C, PES-RB-0.5, PES-RB-2, PES-RB-5, PES-WSD-0.5, PES-WSD-2, and PES-WSD-5 corresponding to filler types and loadings and used as substrates in TFC membranes.

2.4. Fabrication of TFC-FO membranes

The fabrication of the PA layer on top of the porous substrate was performed via the IP method. According to previous studies, optimum conditions were selected to yield the maximum permeate flux and salt rejection related to the PA layer [51,52]. In this regard, the MMMs were firstly soaked in an aqueous MPD solution (2.0 wt%) containing water and ethanol (volume ratio of 1:1) for 120 s. Then, the excess MPD solution was removed from the MMM surface using a rubber roller, and the membrane was then immediately immersed in an organic TMC

solution (1.0 wt%) containing n-hexane for 60 s. The complete polymerization reaction between MPD and TMC monomers at the water/n-hexane interface formed an ultra-thin PA layer on top of the substrates. Finally, the resulting TFC membranes were dried at 85 °C for 5 minutes and stored in DI water before use. These membranes were labeled as TFC-C, TFC-RB-0.5, TFC-RB-2, TFC-RB-5, TFC-WSD-0.5, TFC-WSD-2, and TFC-WSD-5 based on corresponding MMM type.

2.5. Water uptake measurements on RB and WSD

The water uptake test was performed to evaluate the impact of the physicochemical properties of RB and WSD particles in water adsorption. First, the as-prepared particles were dried in a vacuum oven at 75 °C for 4 h. Then, the particles were cooled down to room temperature (24 ± 0.5 °C) before weighing. After immersing in liquid water at room temperature, samples were taken out at specific time intervals and the surface moisture was removed by a large cavity filter paper before weighing. The water uptake was calculated by the following equation:

$$\text{Water uptake (\%)} = \frac{m_w - m_d}{m_d} \times 100 \quad (1)$$

where, m_w and m_d are the weights of the wet and dry samples, respectively.

2.7. Measurement of TFC membrane intrinsic separation properties in the RO process

To determine the mass transfer properties of TFC membranes, including pure water permeability (A), salt flux (B), and salt rejection (R), a cross-flow RO filtration test unit was utilized [53]. All tests were performed under a constant cross-flow velocity (20 cm/s) and temperature (22±0.5 °C) to restrict the number of variables in the system. The A-value was measured under three different pressures (50, 100, and 150 psi) using DI water FS. With the

obtained volumetric pure water flux (J) for each applied pressure (ΔP), the A-value for each TFC membrane can be calculated by the following equation [54]:

$$A = \frac{J}{\Delta P} \tag{2}$$

Also, to evaluate the salt rejection percentage (R%), a feed solution of 20 mmol/L NaCl was utilized under 2.5 bar and for 5 h. According to the experiments, the R-value was calculated by the following equation [54]:

$$R(\%) = \left(1 - \frac{C_P}{C_F}\right) \times 100 \tag{3}$$

where C_F and C_P are the concentrations of salt in the feed and permeate side, respectively. After calculating the values of A and R, the B-value of TFC membranes can be determined using these parameters by the following equation [54]:

$$B = \left(\frac{1 - R}{R}\right)[A(\Delta P - \Delta\pi)] \tag{4}$$

where Δπ is the osmotic pressure difference across the membrane.

2.8. Measurement of TFC membrane performance in FO mode

The performance of TFC FO membranes was evaluated in a cross-flow laboratory-scale test unit. The membrane area was approximately 30 cm^2. A thin spacer was placed on the FS side to promote mixing and reduce the concentrative external concentration polarization (CECP). NaCl solutions at concentrations of 0.5 and 2 M (as DS) and also DI water and Caspian seawater (as FS) were used in all FO experiments. The initial volumes of DS and FS were 2.5 and 2 L, respectively. Two diaphragm pumps (Headon, 2.2 LPM) were used to pump the DS and FS. Two adjustable flow meters were utilized on both DS and FS flow paths to fix the

velocity on 20 cm/s. For more accuracy, the temperature of both DS and FS was adjusted at 25 °C. The DS container was placed on an electronic scale (Mettler Toledo) to record weight changes at specified intervals. The starting point of the recording (t=0) was immediately after all air-bubbles in the test chamber were removed. In this study, all experiments were performed in FO mode. According to the absolute volume change of the FS (ΔV_{feed}) over a specified time interval (Δt) during FO experiments and membrane-active area (A_m), FO water flux (J_w) can be calculated by the following equation:

$$J_w = A(\pi_{DS} - \pi_{FS}) = \frac{\Delta V_{feed}}{A_m \times \Delta t} \quad (5)$$

To calculate the average reverse salt flux (J_s), a conductivity meter (Lutor, WA-2017SD) was used to record and monitor the conductivity of both FS and DS at specific time intervals. Based on the conductivity increment of the FS, the J_s was calculated using the following equation:

$$J_s = \frac{V_t \cdot C_t - V_0 \cdot C_0}{A_m \times \Delta t} \quad (6)$$

where C_t and C_0 are the final and initial (at time) salt concentrations in the FS and V_t and V_0 are the final and initial (at time) volume of the FS.

2.9. Determination of structural parameters

As mentioned in section 1, there is an acceptable agreement that the intrinsic structural parameter, S, affects the severity of the DICP phenomenon. Accordingly, the SL creates resistance to diffusion of the DS in FO membranes operating in the FO mode and reduces the effective osmotic pressure driving force across the AL, which results in water flux decrement. In FO mode the S-value of the TFC FO membranes was determined using the following equation [55]:

$$S = \frac{D}{J_w}\left[\ln \frac{A\pi_{DS} + B}{A\pi_{FS} + J_w + B}\right] \quad (7)$$

where D is the salt diffusion coefficient and π_{draw} and π_{feed} are the bulk osmotic pressures of the DS and FS, respectively. Also, the DS resistivity to diffusion (K) within the SL can be calculated by the following equation [50]:

$$K = \frac{S}{D} \quad (8)$$

2.5. Characterization

To investigate the chemical groups, the FTIR spectrometer (Thermo Nicolet Avatar 370, USA) was used to indicate various functional groups presenting in RB and WSD particles and MMMs. The particle size of the RB and WSD samples was determined by DLS (Shimadzu sald-2101). The membrane structural morphology and particle morphology was evaluated by FESEM (JEOL JSM-6700F). FESEM images can provide a better understanding of the impact of loading RB and WSD particles on the structure of the substrate. The surface roughness of the membranes was evaluated by AFM (Easyscan2 Flex AFM, Switzerland). The surface roughness of the substrate has an essential impact on the formation of the PA layer and its properties. The surface hydrophilicity of the substrates was analyzed with DI water using CA measurement (KRUSS G10, Germany). Membrane hydrophilicity has a significant advantage in the FO process to increase water flux and reduces the DICP. The membrane thickness was determined by a digital micrometer (Carl Mahr D7300, Germany). Although high mechanical strength is not required in FO systems, low mechanical strength develops with increasing the porosity of the support layer. Therefore, the mechanical strength properties were measured with a vertical universal tensile testing machine SANTAM (STM–20, Korea) equipped with a 6 N of load cell at room temperature. The elemental composition of the PA active layer was

investigated by XPS (Bestec, Germany). The following equation was used to calculate the degree of cross-linking of the PA active layer [56]:

$$\frac{O}{N} = \frac{3m + 4n}{3m + 2n} \qquad m + n = 1 \tag{9}$$

where *n* and *m* are the relative fractions of the linear part and cross-linked part, respectively.

The developed SHN1 method based on the linear regularization theory was used to evaluate the average pore size of substrates from the wet-flow state curve [57,58]. The membrane bulk porosity (ε) was based on the weight change before and after immersing in DI water (24 h in this case) and calculated by the following equation [59]:

$$\varepsilon = \frac{(m_{wet} - m_{dry})/\rho_w}{(m_{wet} - m_{dry})/\rho_w + (m_{dry}/\rho_p)} \tag{10}$$

where ρ_p and ρ_w are the densities of polymer and water, respectively, while m_{wet} and m_{dry} are the weights of the wet and dry substrates. The reported results of all tests are the average of three randomly selected locations or three different standard measurements.

3. Results and discussion

3.1. Characterization of RB and WSD

3.1.1. Physicochemical properties

FTIR analysis was used to verify the structural nature of RB and WSD particles in this study. With the IR spectrum, the main functional groups present on the surface can be identified. As

shown in Fig. 1, the IR peaks at 3424 cm^{-1} and 3421 cm^{-1} correspond to O-H stretching vibrations of cellulose, hemicelluloses, lignin and (probable) absorbed water in RB and WSD, respectively. The peak at 2925 cm^{-1}, shows the C-H stretching vibrations of methyl and methylene groups in both particles. The peaks at 1737 cm^{-1} and 1729 cm^{-1} in RB and WSD, respectively, are attributed to the carbonyl group (C=O) of acetyl ester in hemicellulose and carbonyl aldehyde in lignin. Also, the bands in the range of 1000-1300 cm^{-1} are characteristic of C-O stretching vibration of carboxylic groups in anhydroglucose ring, hemicelluloses and, lignin in both RB and WSD particles. Similar results can be found in the literature [48,60]. Based on the obtained results in this study, we can say that the chemical structure of RB and WSD is very close together. Therefore, it is essential to investigate the physical and structural differences between these two particles.

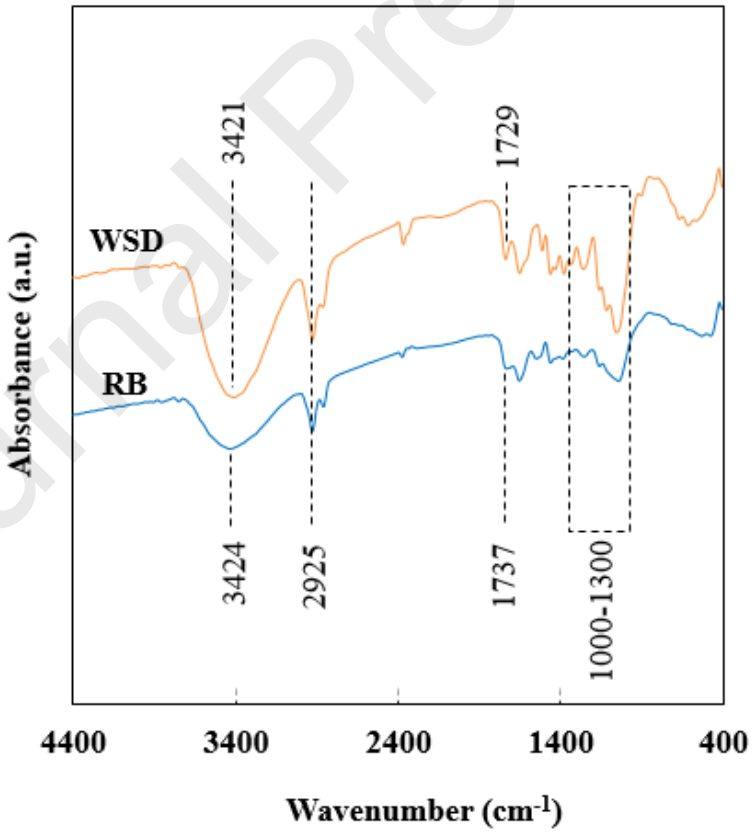

Fig. 1 FTIR analysis of RB and WSD samples.

FESEM images of RB and WSD particles are shown in Fig. 2. The results show that none of the RB and WSD particles has a distinct morphology. However, the main difference between these two samples is their particle size. The DLS analysis presented in Fig. 3 shows this difference in particle size numerically. According to Fig. 3, the average sizes of RB and WSD particles are around 1 and 5 µm, respectively. Since the process of preparation and milling time for RB and WSD were quite similar, the smaller particle size of RB would indicate the softer structure of RB compared to WSD.

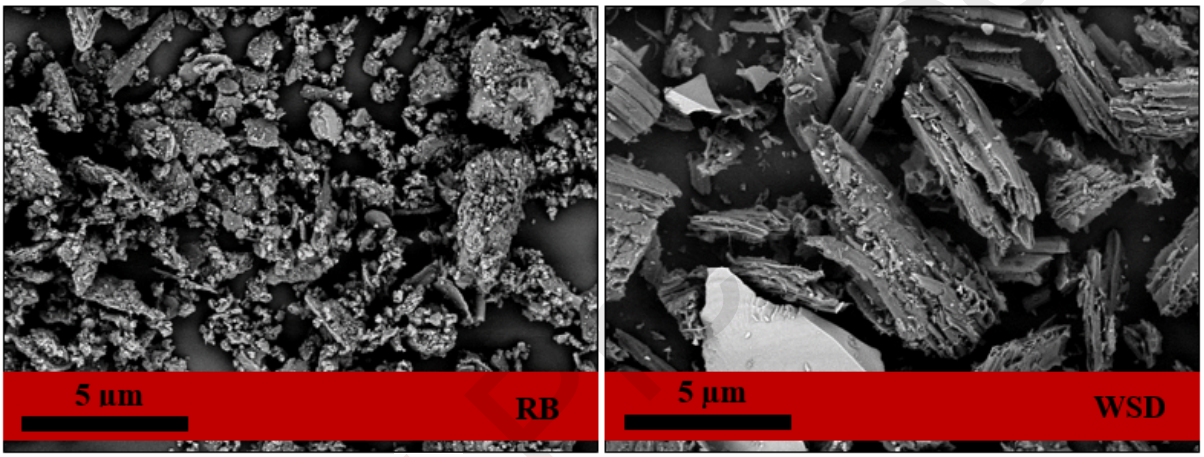

Fig. 2 FESEM images of RB, and WSD samples.

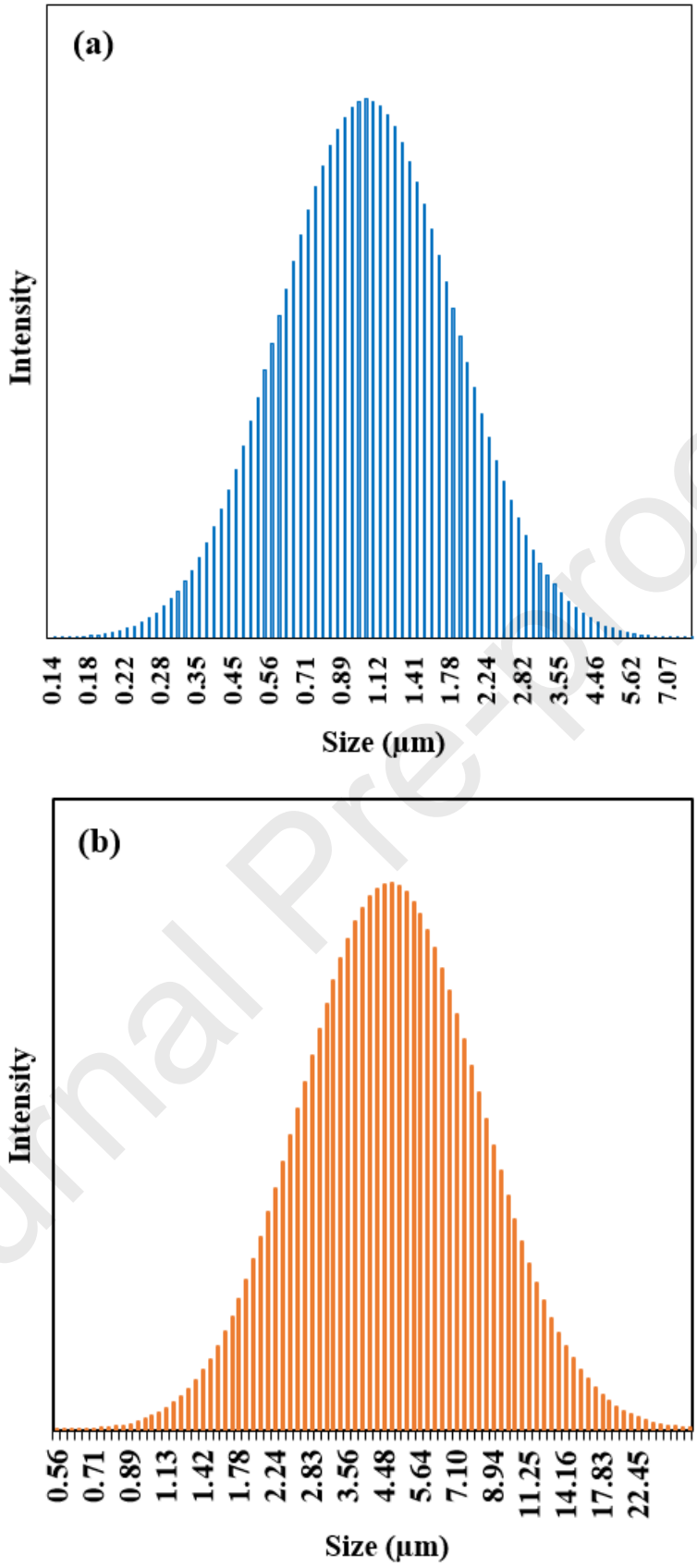

Fig. 3 DLS result of (a) RB, and (b) WSD.

3.1.2. Water uptake

One of the most critical factors for particles used in the SL of the TFC FO membranes to reduce the DICP phenomenon is their ability to water uptake. For this purpose, the water uptake experiment for both RB and WSD particles was performed (Fig. 4). According to Fig. 4, the saturated water uptake for RB particles is higher than WSD particles. Considering the high chemical similarity of RB and WSD, it can be attributed to the smaller size of RB particles, as shown in FESEM images and DLS results, which provided more surface area for these particles. But it is evident that in the first 720 seconds of the experiment, the water uptake of WSD samples was equal or higher than that of the RB samples. A reasonable explanation for this phenomenon is that smaller particles are more susceptible to agglomeration, which can reduce the specific surface area and accessible pores. However, this is a temporary behavior and water will eventually reach all the particles and total real surface area. So, it can be predicted that probably, incorporation of RB particles in the SL of TFC FO membranes, has led to more water uptake capacity and a more porous structure that has reduced the S-value and DICP phenomenon.

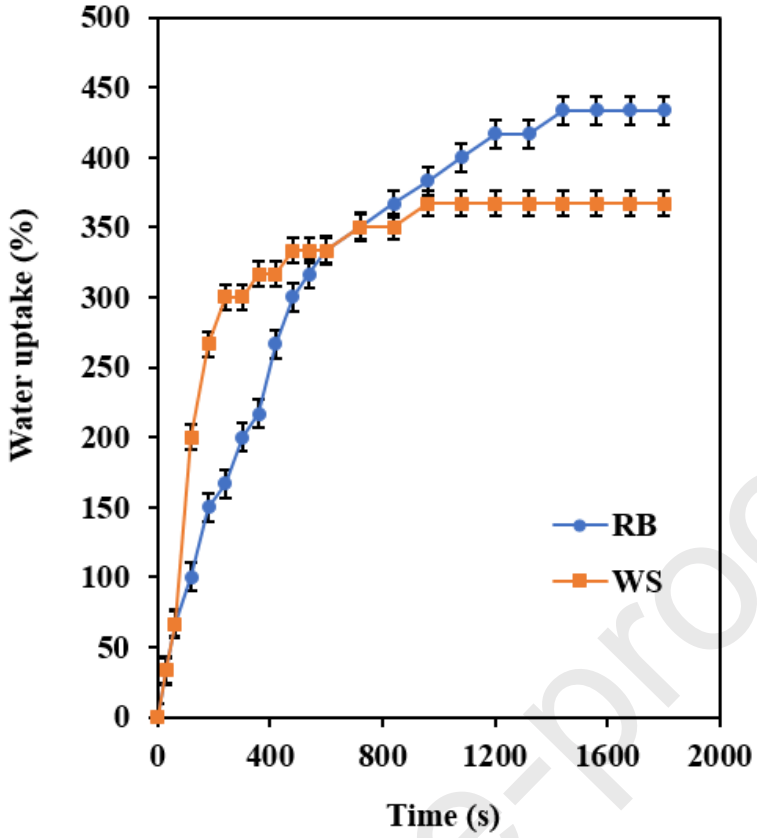

Fig. 4 Water uptake of RB, and WSD particles.

3.2. Characterization of MMMs

3.2.1. Physicochemical properties

The FTIR analysis was performed to identify the impact of the percentage loading of RB and WSD on the chemical composition of the MMM surface and investigating the presence or absence of new functional groups resulting from the chemical reactions (Fig. 5). According to obtained results, the IR peaks of neat PES (PES-C) at 1585 cm^{-1} and 1486 cm^{-1} are attributed to aromatic in-plane ring bend stretching vibration (CH_3-C-CH_3 stretching). The peak observed at 1403 cm^{-1} is due to C=C aromatic ring stretching. Peaks at 1311 cm^{-1} and 1243 cm^{-1} correspond to asymmetric O=S=O stretching vibration and asymmetric C-O-C stretching (vibration of the aryl-O-aryl group), respectively. Peaks at 1159 cm^{-1} and 833 cm^{-1}, is characteristic of O=S=O symmetric stretching vibration and hydrogen deformation of para-substituted phenyl groups' in-phase out-of-plane, respectively. Finally, peaks in the range of

2900-3100 cm^{-1} can be assigned to aliphatic C-H stretching vibrations. Similar results can be found in other literature [12,26]. In the case of MMMs, the absorption bands of PES and RB or WSD particles were observed in all composite membranes with slight shifts in peaks' frequencies. According to the results, due to similar chemical bonds, relative overlapping between the bands of the RB or WSD particles and PES is observed. As shown in Fig. 5, there is no new peak in the IR spectrum of the MMMs comparing with the neat PES and pure RB or WSD particles, which indicates that there is no chemical reaction between the RB and WSD particles and the PES polymer. The slight shift observed in the spectrum of MMMs in comparison with PES-C, especially at particle loadings of 2 and 5 wt%, can be attributed to the incorporation of particles into the polymer chains and their elongation [48].

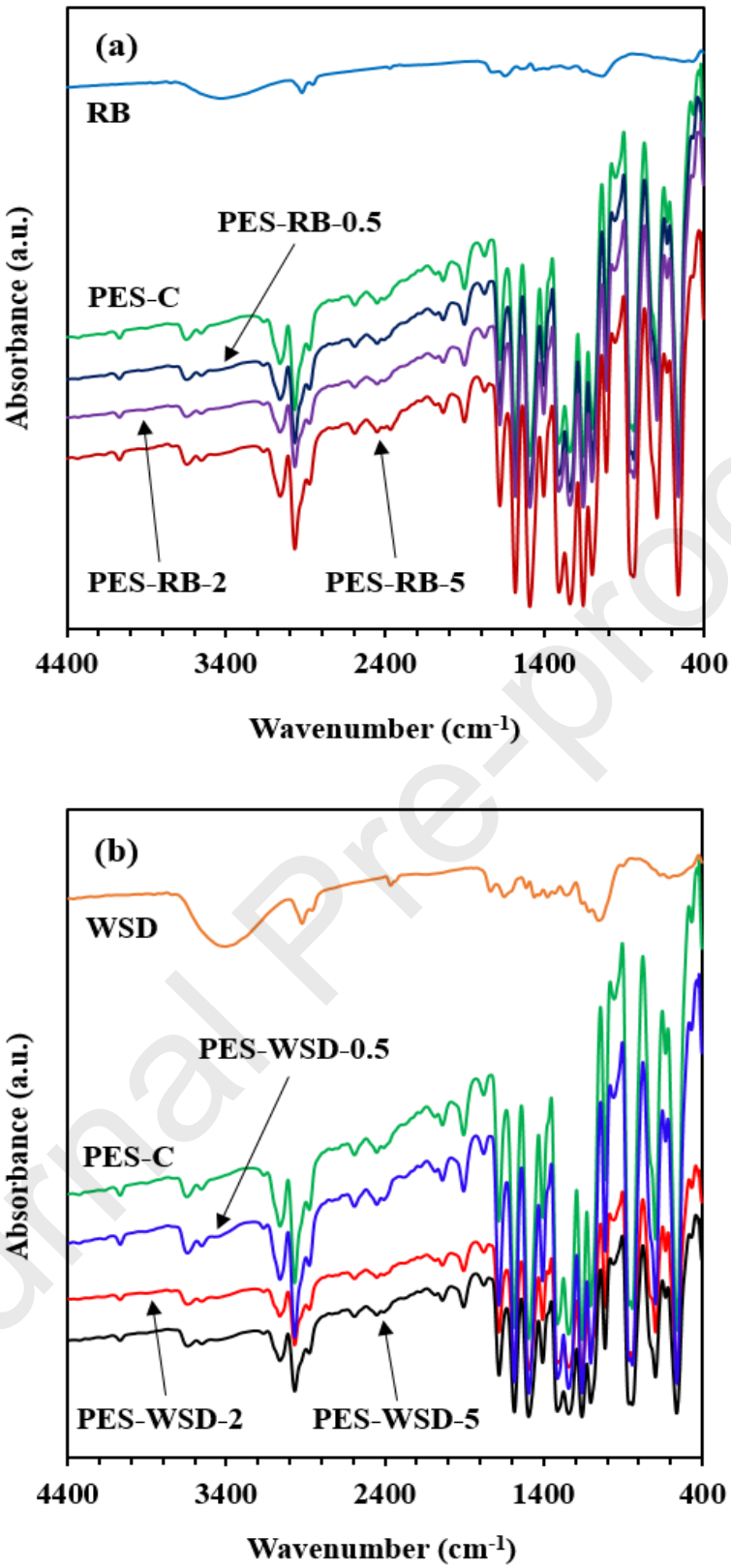

Fig. 5 FTIR spectra of PES-based SLs with various loading of (a) RB, and (b) WSD.

Table 2 also shows the structural properties of all MMMs, such as porosity (ε), thickness (t), contact angle (CA), mean pore size (d_{avg}), and diffusion factor ($\varepsilon d_{avg}^2/4t$). According to Table 2, the average thickness of all MMMs is in the range of 38-50 μm. However, under the same conditions, the thickness of the membranes made with RB particles is lower than those made with WSD particles, and this is probably due to the softer structure of the RB particles. The results also show that the overall porosity of all MMMs increased by incorporating RB or WSD particles in the support layer. Carefully in the trends of results obtained, it is evident that as the loading percentage of RB or WSD particles increases, the overall porosity increases. However, the effect of using RB particles to increase the total porosity of the SLs is higher than that of WSD particles, which is attributed to the smaller particle size of RB particles.

Table 2: The general properties of all MMMs with different type and loading of RB and WSD.

Membrane code	Thickness t (μm)	Porosity ε (%)	Contact Angle CA (°)	Mean Pore Size d_{avg} (nm)	$\frac{\varepsilon d_{avg}^2}{4\delta} \cong \frac{\varepsilon d_{avg}^2}{4t}$
PES-C	50 ± 1	63 ± 1	59 ± 3	36.39	4.17
PES-RB-0.5	44 ± 2	73 ± 3	58 ± 1	35.74	5.30
PES-RB-2	40 ± 3	77 ± 2	54 ± 1	26.79	3.45
PES-RB-5	38 ± 2	91 ± 3	51 ± 3	22.35	2.99
PES-WSD-0.5	46 ± 2	69 ± 2	57 ± 1	35.11	4.62
PES-WSD-2	43 ± 3	74 ± 2	53 ± 2	22.25	2.13
PES-WSD-5	41 ± 2	82 ± 2	49 ± 3	18.02	1.62

The cross-section morphological structure of the asymmetric PES-C and corresponding MMMs prepared in low and high loading of RB and WSD particles were characterized by analyzing the FESEM images (Fig. 6). As can be seen in Fig. 6, the neat PES SL (PES-C) has a typical asymmetric structure that was expected. As mentioned earlier, Fig. 6 shows the cross-section images of MMMs in low and high loadings of RB and WSD particles. The results show that both RB and WSD particles are well dispersed in the polymeric matrix. By adding both RB and WSD particles in PES, the structure of the PES-C membrane cavities will undergo some changes. The formation of some macropores in the structure of MMMs is evident. Also,

the larger particle size of WSD is apparent in the FESEM images of MMMs. This observation confirms the results presented in Figs. 2 and 3.

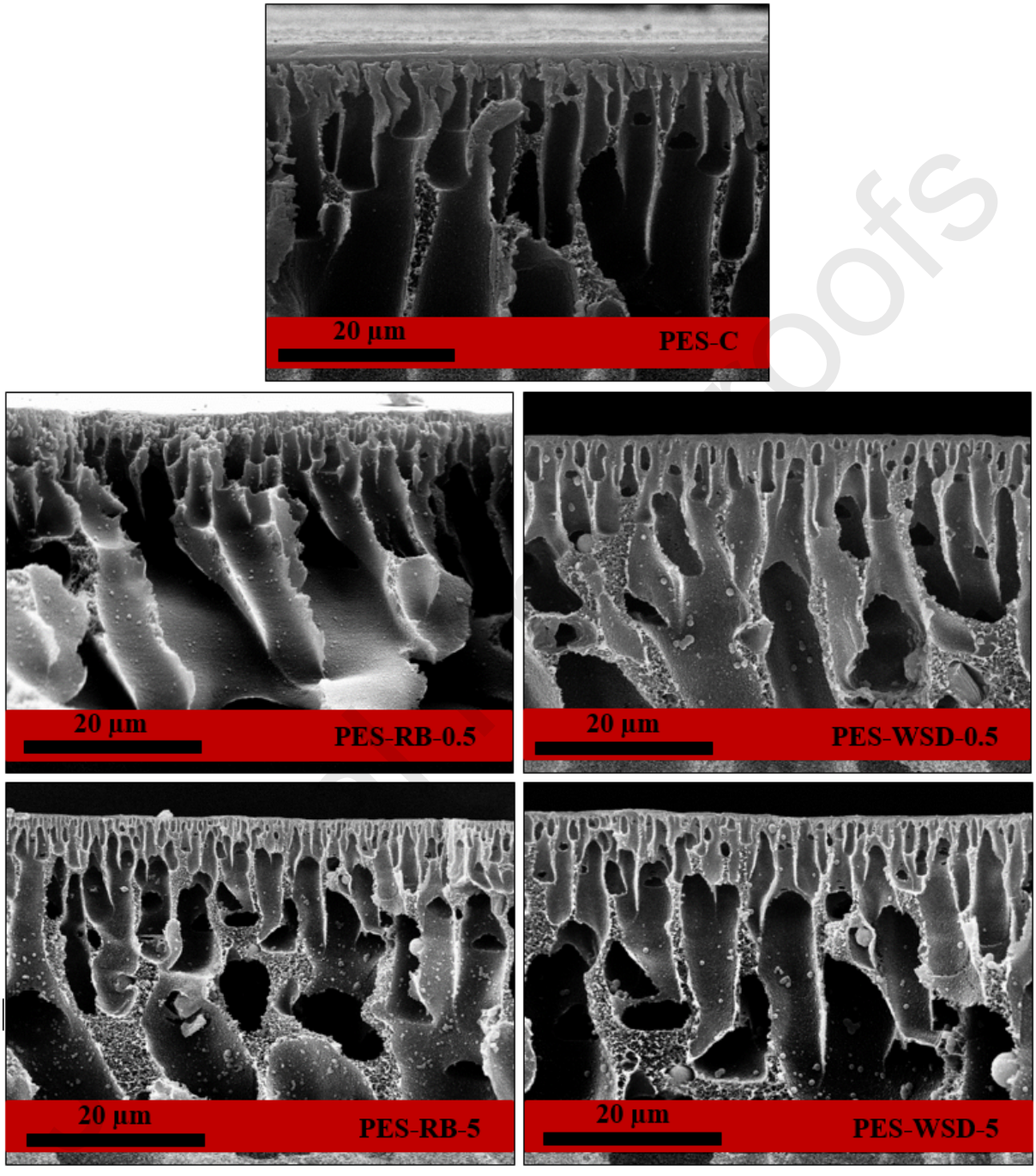

Fig. 6 The cross-section morphologies of prepared MMMs.

Since the properties of the SL surface affect the formation of PA layer characteristics such as the cross-linking degree and thickness, AFM analysis was used to provide an insight how the neat PES membrane surface roughness changes with RB and WSD loadings. Accordingly, the

roughness factors and AFM 3D images of all prepared SLs are shown in Table 3 and Fig. 7. According to obtained results, the surface roughness was increased by adding both RB and WSD particles. It is also clear that under the same conditions, the MMMs fabricate with WSD particles are rougher than those made with RB particles. The larger particle size of WSD along with their coarser nature are some of the reasons for these results.

Table 3: Surface roughness parameters of MMMs.

Membrane code	R_a (nm)	R_q (nm)
PES-C	6.5	8.1
PES-RB-0.5	7.01	9.03
PES-RB-2	8.07	10.19
PES-RB-5	8.81	10.93
PES-WSD-0.5	7.27	9.31
PES-WSD-2	8.47	10.65
PES-WSD-5	9.37	11.39

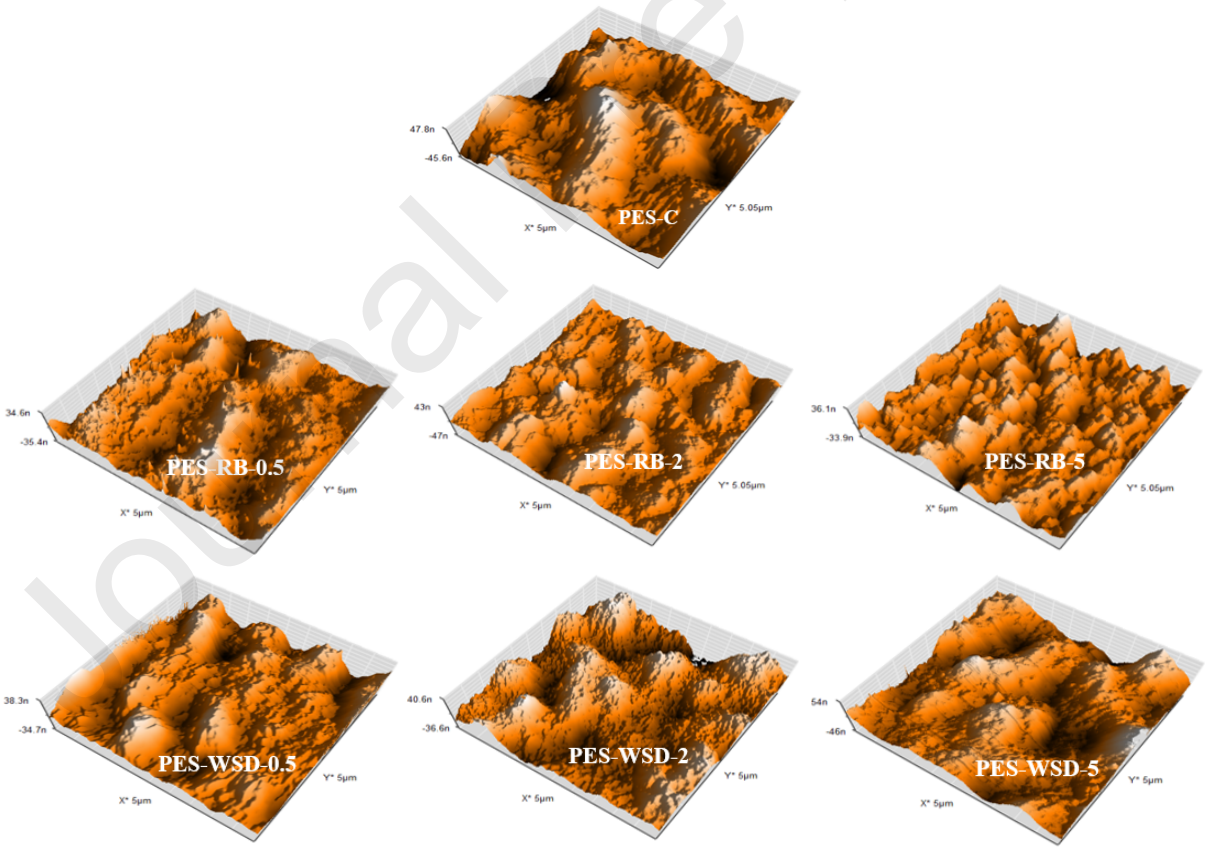

Fig. 7 3D AFM images of the prepared MMMs.

Interestingly, the SLs modified with RB and WSD were found to have smaller water contact angle (CA) than the neat PES-based membrane, as shown in Table 2 due to the high hydrophilicity of WSD/RB particles. Water uptake experiments showed that RB particles are more hydrophilic than WSD particles. However, the results of the CAs showed that under the same conditions, the membranes fabricate with WSD have smaller CA. The reason for this contradiction is the surface roughness. As listed in Table 3, the MMMs made with WSD particles are rougher than those made with RB particles. According to the Wenzel equation, for wettable surfaces (CA <90°), the surface CA decreases with increasing the surface roughness [61]. Thus, the surface roughness of the MMMs, particularly in WSD-based MMMs, increases the hydrophilicity, which can eventually result in a decrease of CA of SLs.

The impact of the incorporation of WSD and RB particles on the mechanical properties, including elongation at break and tensile stress of all prepared SLs is shown in Fig. 8. For a specific polymer, the added particles (filler) strongly affected the mechanical properties of the prepared MMMs, and it was dependent on the physicochemical properties of membranes such as the percentage of loading, particle size, agglomeration of particles, and the affinity between polymers and fillers [48]. Accordingly, the results presented in Fig. 8 show that the final amounts of elongation at break and tensile strength of prepared MMMs are decreased with increasing the percentage loading of WSD or RB particles. Reduction of flexibility and plasticity of the PES chains after the presence of WSD and RB particles in the polymeric matrix shows no considerable affinity between WSD or RB particles and PES chains (such as chemical bonds), and formation of macropores in the prepared MMMs would justify these results [48,62].

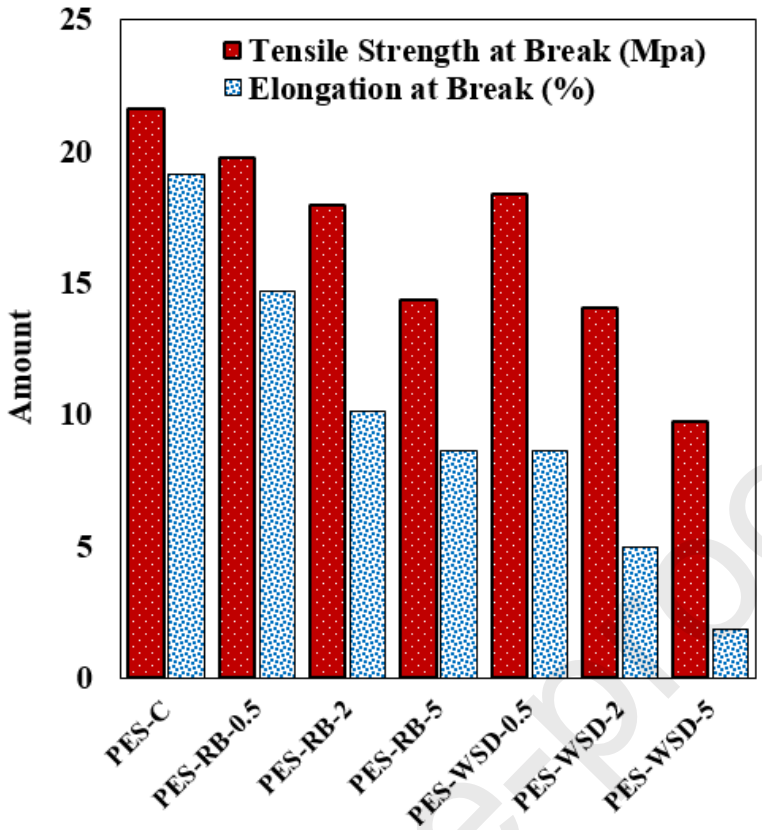

Fig. 8 Elongation at break and tensile strength of prepared MMMs.

3.2.2. Intrinsic separation property

The effect of loading of WSD and RB particles on the pure water permeation (PWP) and the diffusion factor ($\varepsilon d_{avg}^2/4t$) of the MMMs is shown in Fig. 9. As shown in Fig. 9, the PWP values are higher for MMMs than those obtained for the neat PES membrane and reached a maximum amount at 0.5 wt% loading percentage.

Given that the overall porosity of the all prepared MMMs increased with increasing the percentage of additives, the obtained results for the PWP seem a little unreasonable. Nevertheless, it should be noted that the values obtained for PWP are not only dependent on the overall porosity. PWP values depend on two chemical and physical factors [24,49]. In this study, the only chemical factor is the CA, while the most important physical factor is the diffusion factor ($\varepsilon d_{avg}^2/4t$). The results presented in Table 2 show that the CA values are not

very significantly different between these six SLs. The mismatch between the trends of changing PWP and CA also indicates that the chemical factor is not determinant (at least in this study). However, Fig. 9 shows that the trends in PWP and diffusion factor changes are entirely consistent. Accordingly, owing to the more significant diffusion factors in PES-WSD-0.5 and PES-RB-0.5 SLs, the higher PWP values obtained for these two SLs are reasonable. According to the results presented in Fig. 9, it can be said that the obtained PWP values for the SLs containing RB particles are higher than the corresponding SLs containing WSD particles. These results are also related to the trend of changing diffusion factors.

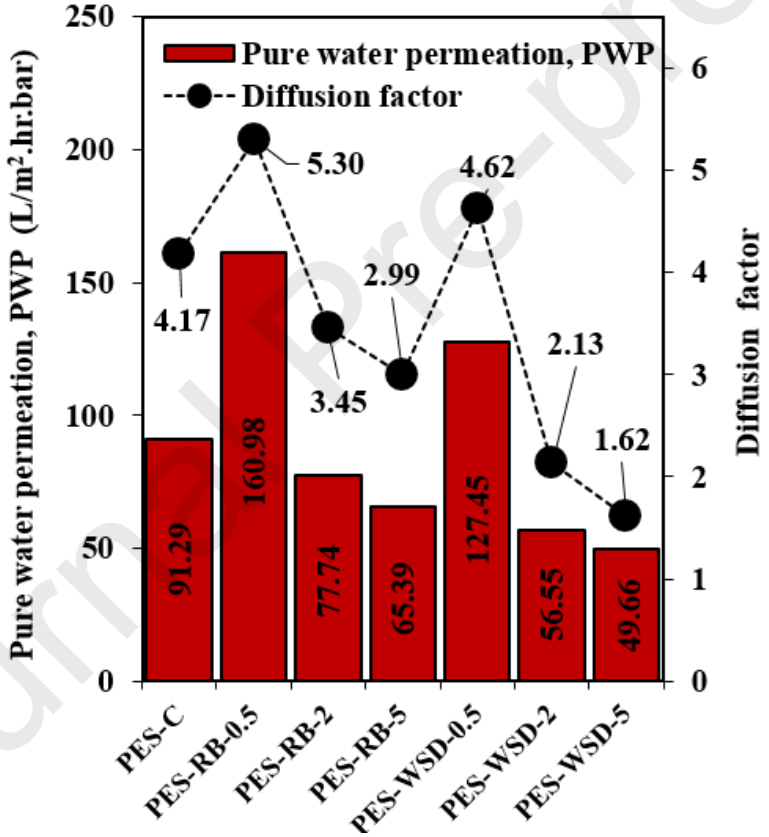

Fig. 9 Pure water permeation and diffusion factor of all prepared MMMs.

3.3. Characterization of TFCs

3.3.1. Characterization and separation performance

The performance of the TFC membranes depends on the properties of both AL and SL. Accordingly, the SL information was examined in the previous sections. For further investigation, in this section, contact angle (θ), thickness (L), salt rejection (R), and the ratio of transport parameters (B/A) for all TFC membranes, are listed in Table 4. Fig. 10 illustrates the intrinsic water permeability (A) and salt flux (B) of all TFC membranes. According to the obtained results, the RB and WSD particles led to the formation of macro voids in the SL structure and reduction of the membrane thickness, as listed in Table 4. Compared to the TFC-C membrane, a tangible increase in the CA of the PA layer was recorded by adding 0.5 wt% of RB and WSD particles to the SL. For the rest of the TFC membranes, there was a slight decrease in the CA of the PA layer due to adding 2 and 5 wt% of RB and WSD particles to the membranes. This decrease is attributed to the porosity and pore size of the SL and the amount of hydrophilic agent. As shown in Fig. 10, the use of MMMs instead of neat PES membrane, as porous SL fir the TFC membranes caused a non-monotonic behavior of A-values. At low loading percentage (0.5 wt%), the use of PES-RB-0.5 and PES-WSD-0.5 instead of PES-C membrane as SL caused a slight decrease in A-values. Compared to PES-C, increasing the loading percentage of RB and WSD particles into the MMMs increased the A-values (Fig. 10). Also, at all loading percentages, the A-values of WSD-based TFC membranes were higher than the corresponding RB-based TFC membranes. The trend of the obtained results for A-values and change the results with the change of loading percentage (for a specific polymer) as well as the change of additive type (for a constant loading) are in sharp contrast with the PWP results shown in Fig. 9. More likely, this contrasting behavior is due to the differences in the PA layers. Aa a matter of fact, to better understand how the differences in the PA layers can impact on the results, characterization tests on PA layers have to be performed.

Table 4: Summary of the thickness, contact angle, ratio of transport parameters, and salt rejection of all TFC membranes.

Membrane Type	Thickness, L (μm)	Contact angle, θ (°)	B/A (kPa)	Salt rejection, R (%)
TFC-C	51 ± 2	47 ± 1	14.40	97.20
TFC-RB-0.5	45 ± 1	50 ± 2	9.91	98.06
TFC-RB-2	41 ± 1	46 ± 2	14.74	97.14
TFC-RB-5	39 ± 1	45 ± 1	15.23	97.04
TFC-WSD-0.5	47 ± 2	49 ± 2	10.59	97.93
TFC-WSD-2	44 ± 1	43 ± 3	15.82	96.93
TFC-WSD-5	42 ± 2	43 ± 1	17.52	96.61

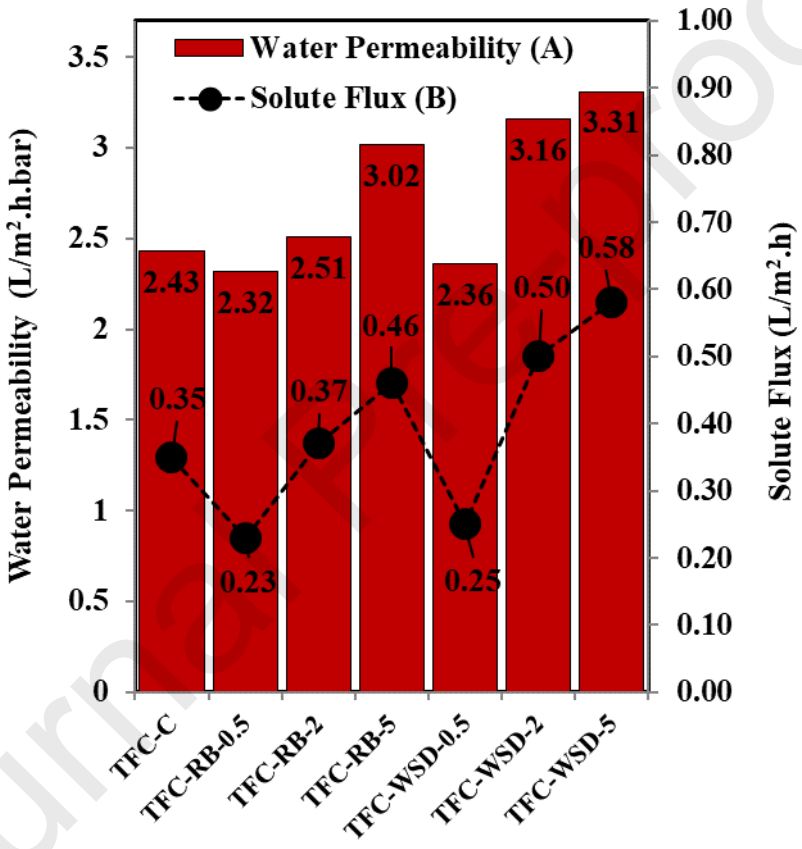

Fig. 10 Water permeability (A) and solute flux (B) of all TFC membranes.

For the characterization of the PA layer, the XPS analysis was performed on the top surface of the TFC membranes to calculate the crosslinking degree of the PA layer on all SLs. Table 5 listed the elemental composition of the PA layer for each TFC membrane. The results show that by incorporation of RB and WSD particles into the neat PES matrix, the degree of crosslinking of the PA was changed. In describing the IP reaction process, it can be said that

the MPD monomer diffuses from the SL pores to reach the aqueous/organic interface in which the TMC monomer exists, then the PA layer forms through the chemical reaction between MPD and TMC monomers [51,52]. The diffusion rate of the MPD monomer depends on two chemical and physical factors, which will be examined separately. In the case of chemical factors, the hydrophilicity of the SLs affects the diffusion rate of the MPD monomer and the formation of the PA layer. In effect, hydrogen bonding between the MPD and the hydrophilic groups prevents the facile diffusion of the MPD to the surface of the membrane, and it can limit the formation of the PA layer and reduces the degree of crosslinking. For physical factors, the diffusion rate of the MPD monomer is proportional to $\varepsilon d_{avg}^2/4t$ factor [28]. Besides, some TMC may diffuse into the cavities and form precipitated PA in the pores [28]. Accordingly, the formation of the initial PA layer can also act as a barrier layer against the diffusion of the MPD and limits the further growth of the PA layer. This phenomenon depends on several factors, such as the SL pore size and polymerization time, and it can be only confirmed by examining the results of the degree of crosslinking or A-values. According to obtained results, the CA of MMMs decreased in the order of PES-C > PES-RB-0.5 > PES-WSD-0.5 > PES-RB-2 > PES-WSD-2 > PES-RB-5 > PES-WSD-5. In addition, the factor was decreased in the order of PES-RB-0.5 > PES-WSD-0.5 > PES-C > PES-RB-2 > PES-RB-5 > PES-WSD-2 > PES-WSD-5. Finally, the results listed in Table 5 show that the degree of crosslinking value was decreased in the order of TFC-RB-0.5 > TFC-WSD-0.5 > TFC-C > TFC-RB-2 > TFC-RB-5 > TFC-WSD-2 > TFC-WSD-5. These results show that the formation of the PA layer is influenced mostly by physical factors. In effect, given that the CA values for all the SLs do not differ significantly. It is evident from the results that the hypothesis of PA layer formation inside the pores is incorrect.

The degree of crosslinking and the quality of the PA layer is critical in determining the rejection of the salts [63]. The B/A ratio is a decisive factor that describes the membrane selectivity [29].

According to results presented in Tables 4 and 5, it is clear that the trends of changes for B/A ratio and degree of crosslinking are inversely proportional. In other words, by increasing the degree of crosslinking of the PA layer, the R-values also increased. Depending on the membrane application, the best membrane would be selected as a tradeoff between water permeability and salt rejection parameter.

Table 5: XPS analysis of TFC membranes fabricate by various types of substrates.

Membrane Type	O (%)	N (%)	C (%)	O/N	O/C	N/C	Degree of cross-linking (%)
TFC-C	18.36	12.08	69.56	1.52	0.26	0.17	38
TFC-RB-0.5	14.54	11.08	74.38	1.31	0.20	0.15	59
TFC-RB-2	18.97	12.17	68.86	1.56	0.28	0.18	34
TFC-RB-5	19.53	12.18	68.29	1.60	0.29	0.18	30
TFC-WSD-0.5	14.08	10.30	75.62	1.37	0.19	0.14	53
TFC-WSD-2	20.04	12.23	67.73	1.64	0.30	0.18	27
TFC-WSD-5	20.62	12.41	66.97	1.66	0.31	0.19	25

To further investigate the top-surface morphology of all TFC membranes, characterization by FESEM was performed, and the results are presented in Fig. 11. According to the obtained results, the top-surface of all TFC membranes presented typical ridge and valley structures, indicating that the selective PA layer was successfully formed on the top surface of all SLs. According to the images presented in Fig. 11, it is evident that the PA layer for the PES-RB-0.5 and PES-WSD-0.5 membranes has a more compact structure than the other TFC membranes. However, the PA layer for the rest of the MMM-based TFC membranes has a less compact structure than the neat PES-C membrane. Given that the compact structure of the PA layer and the degree of crosslinking are proportional to each other, it can, therefore, say that the results presented in Table 5 as well as the images presented in Fig. 11 confirm each other.

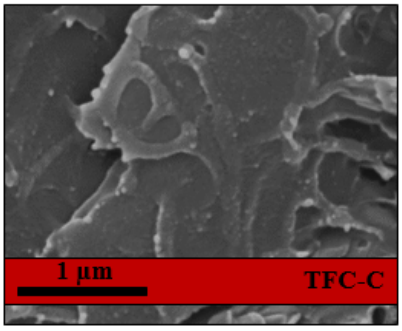

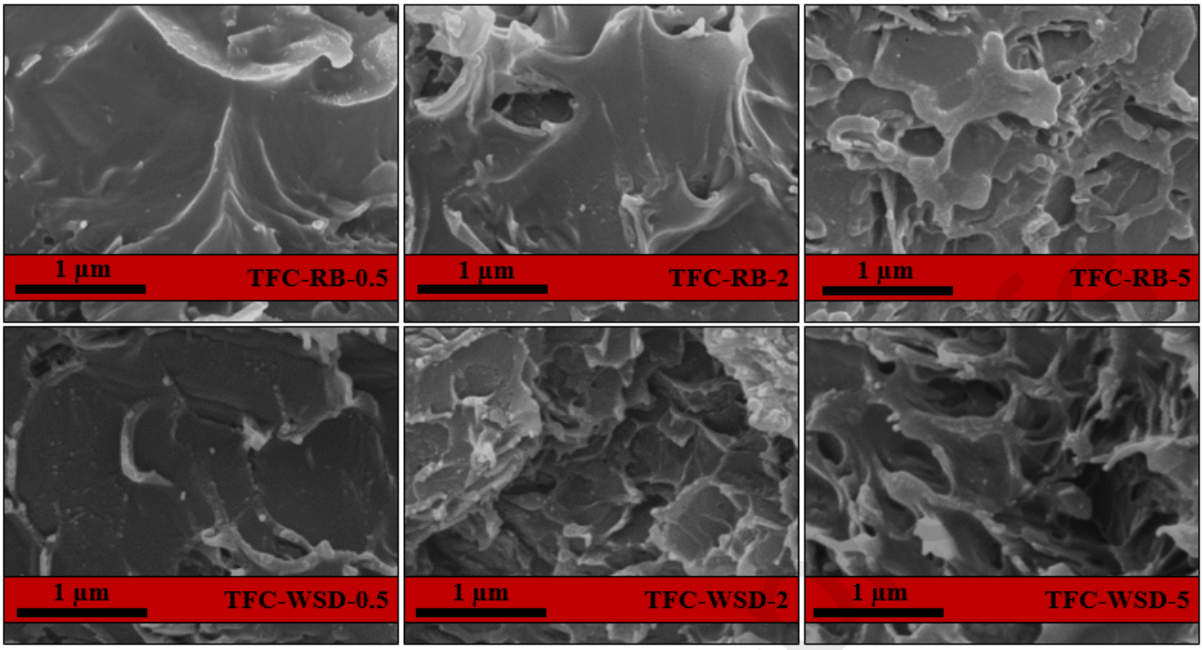

Fig. 11 Top surface FESEM images of the prepared TFC membranes.

3.3.2. Performance of the FO membrane

The performance of the FO membrane was evaluated in terms of water flux (J_w) and specific reverse salt flux (J_s/J_w) for all TFC FO membranes in the AL-FS mode (Fig. 12). In all experiments, deionized water was selected as the FS and two NaCl solutions with concentrations of 0.5 and 2.0 M were selected as the DS. As shown in Fig. 12, Jw of the MMM-based TFC FO membranes is higher than those values of the neat PES-C membranes, which is indicative of the positive effect of adding the RB and WSD particles in the TFC FO membranes. After increasing in DS concentration from 0.5 to 2.0 M, the amount of Jw increased because of the more significant driving force created across the FO membranes. Results also revealed that the amount of J_w increased with increasing the percentage loading of particles for both types of RB and WSD TFC membranes. However, this increase in the Jw was higher for the RB-based TFC membranes due to the higher A-value (Fig. 10). However, comparing these results shows that the MMM-based TFC membranes containing 5 wt% of the additives exhibit

inverse behavior. According to the theory of the FO process, increasing Jw (despite decreasing A) is due only to the more increase in active DS osmotic pressure ($\Delta\pi_{eff}$) as a result of increasing the concentration gradient across the membrane (ΔC_{eff})[21]. At first glance, it can be said that according to these facts that TFC-RB-0.5 and TFC-WSD-0.5 membranes have the highest factor (even higher than the TFC-C membrane), such results are justified.

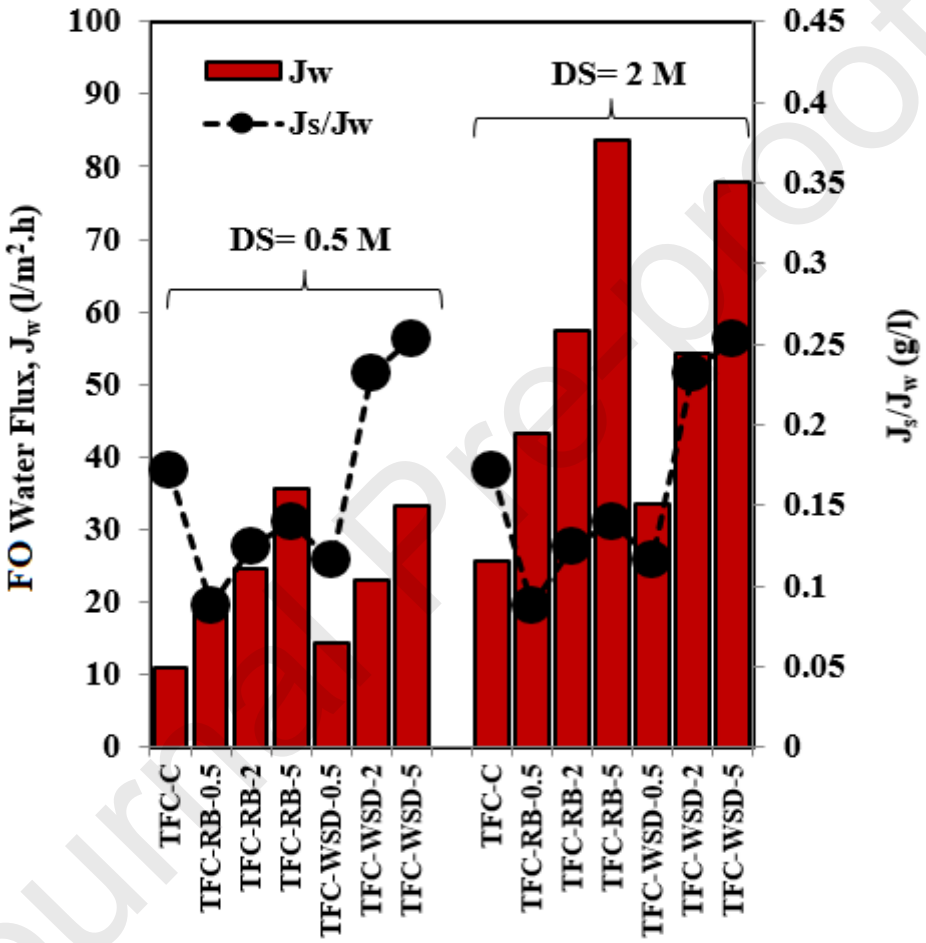

Fig. 12 FO water flux and FO reverse solute flux of the TFC membranes in FO mode.

A detailed investigation of this phenomenon will be possible by analyzing some critical parameters such as structural parameter (S), and tortuosity (τ), as presented in Table 6. As stated in the previous sections, these parameters will be used as direct indicators of the intensity of DICP in the FO SL and can complete the description trends of J_w. According to the obtained results, after incorporation of RB and WSD particles into the neat PES, these parameters are

reduced. Also, the structural parameter for all RB-based TFC membranes is lower than that of corresponding WSD-based TFC membranes. The trends of reducing structural parameters are proportional to the trends of increasing the loading of additives. As such, the diffusion of DS increases in the SL pores by increasing the loading of RB and WSD particles. These results have a direct impact on the osmotic pressure ($\Delta\pi_{eff}$). Fig. 13 shows the values of all TFC FO membranes. As shown in Fig. 13, by increasing the loading of RB and WSD particles, they will increase. Also, by comparing the results presented in Table 6 and Fig. 13, it can be stated that the diffusion of DS into the all RB-based SL pores is more than that of corresponding WSD-based SL pores due to the lower structural parameter of the RB-based SL, especially for the PES-RB-0.5 and PES-WSD-0.5 membranes. The results confirm that the values of the structural parameters and $\Delta\pi_{eff}$ are inversely correlated.

Table 6: Summary of the structural parameters of the TFC membranes.

Membrane Type	S (μm)	Changing S (%)	τ
TFC-C	614.59	---	7.59
TFC-RB-0.5	250.61	-59.22	4.07
TFC-RB-2	155.11	-74.76	2.91
TFC-RB-5	86.72	-85.89	2.02
TFC-WSD-0.5	392.90	-36.07	5.77
TFC-WSD-2	211.21	-65.63	3.55
TFC-WSD-5	111.76	-81.82	2.18

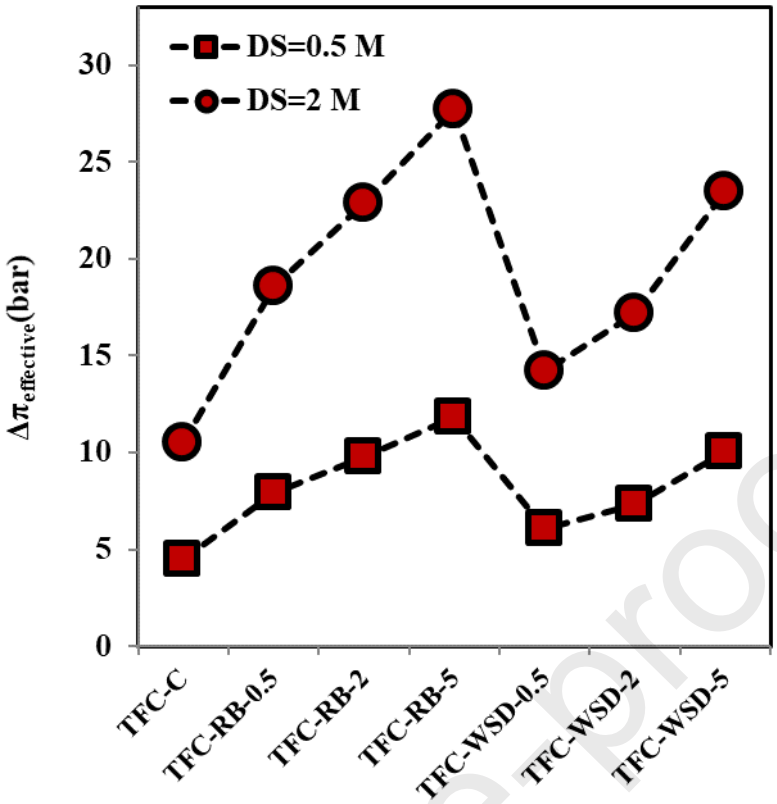

Fig. 13 Values of ΔC_{eff} for all TFC membranes.

The study on the performance of the TFC FO membranes can be complemented by an investigation on the J_s/J_w ratio, which estimates the lost amount of solutes during the FO experiment. The high amount of the J_s/J_w ratio indicates low selectivity. Fig. 12, shows the results of the J_s/J_w factor for all TFC membranes in two DS concentrations. As shown in Fig. 12, the J_s/J_w factor for TFC-RB-0.5 and TFC-WSD-0.5 is lower than the other TFC FO membranes. These two membranes have the highest rejection rate due to the highest degree of crosslinking. In effect, by comparing the results of the degree of crosslinking presented in Table 5 and the results of the J_s/J_w factor presented in Fig. 12, it can be stated that the values of the J_s/J_w ratio and the degree of crosslinking of the PA layer are inversely correlated. Accordingly, the highest J_s/J_w ratio obtained is for the TFC-WSD-5 membrane having the lowest degree of crosslinking.

3.4. Characteristic curve of TFC FO membranes

The characteristic curve presents a trade-off between $J_w/\Delta\pi_{theoretical}$ and J_w/J_s factor, as shown in Fig. 14. The results show that the use of RB and WSD particles into the PES matrix improved the performance of the neat TFC-C membrane. Besides, at lower DS concentrations, the FO performance was increased because of the decreased DICP phenomenon. Given the characteristic curve, it can be safely stated that the TFC membranes fabricate with RB particles are far better than those made with WSD particles. These results show that although the chemical structure of the RB and WSD particles are similar, the differences in physical structure between them will lead to different results in the FO experiment.

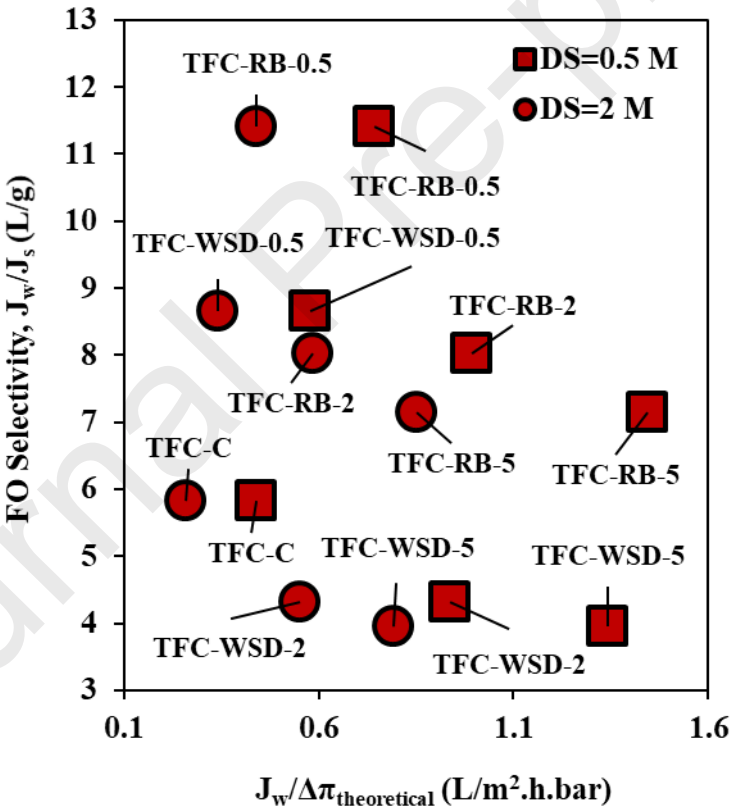

Fig. 14 Comparisons of FO performance of all TFC membranes (orientation: FO mode, FS: DI water, DS: NaCl 0.5 and 2 M).

Fig. 15 compares the performance of all fabricated MMM-based TFC FO membranes with some results reported in the literature [27-29]. A larger circle means better performance in

terms of both J_w/J_s and J_w. The results presented in Fig. 15 shows that the fabricated MMM-based TFC FO membranes in this study perform better than many of the TFC FO membranes made by other researchers [27-29]. The membranes fabricate with RB particles also show great results and are competitive with the TFC FO membranes that have shown outstanding performance. The importance of these results is not only in analyzing the transport parameters and comparing them with other membranes. What is noteworthy is that the MMM-based TFC FO membranes used in this study fabricated with very inexpensive additives. Indeed, after using RB and WSD particles in the neat PES-C membrane, we will see an increase in membrane efficiency, with no additional cost.

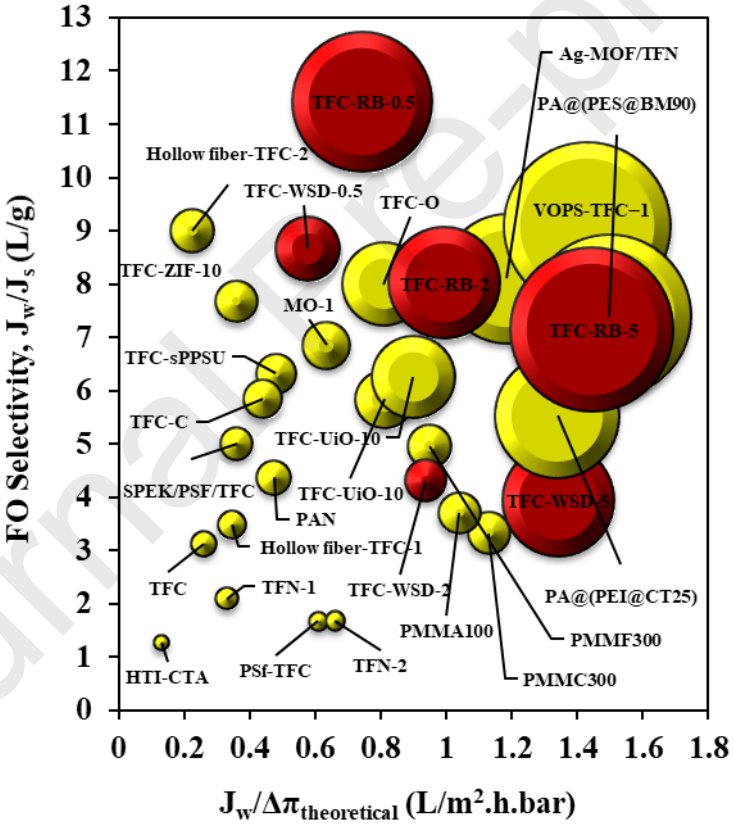

Fig. 15 Comparisons of FO performance of MMM-based TFC FO membrane with other TFC membranes presented in literatures [27-29], (orientation: AL-FS mode, FS: DI water, DS: NaCl 0.5 M, T: 20-25 °C).

3.5. Seawater desalination

In order to investigate the potentials of using the RB and WSD particles with various loading in reducing the DICP phenomenon and desalination performance of the FO process, all of the prepared MMM-based TFC FO membranes were examined using Caspian seawater FS in AL-FS mode. The corresponding results compared to DI water flux presented in Fig. 16. In all experiments, 2 M NaCl solution was used as DS. As shown in Fig. 16, after using the Caspian seawater instead of DI water as the FS, about 28.73% decrease in the J_w was observed for the PES-C membrane. However, after using the fabricated MMM-based TFC membranes, the J_w was decreased about 25.26, 23.88, 23.70, 22.67, 21.92 and 21.45% for TFC-WSD-0.5, TFC-RB-0.5, TFC-WSD-2, TFC-RB-2, TFC-WSD-5, and TFC-RB-5, respectively. The results show that the J_w trends are proportional to the changes in the structural parameters of each membrane (see Table 6). Accordingly, the more positive impact of using the RB-based MMMs is more evident. According to the obtained results can be stated that the reduction rate of J_w was not remarkable, which indicates the good performance of fabricated MMM-based TFC FO membranes in Caspian seawater desalination.

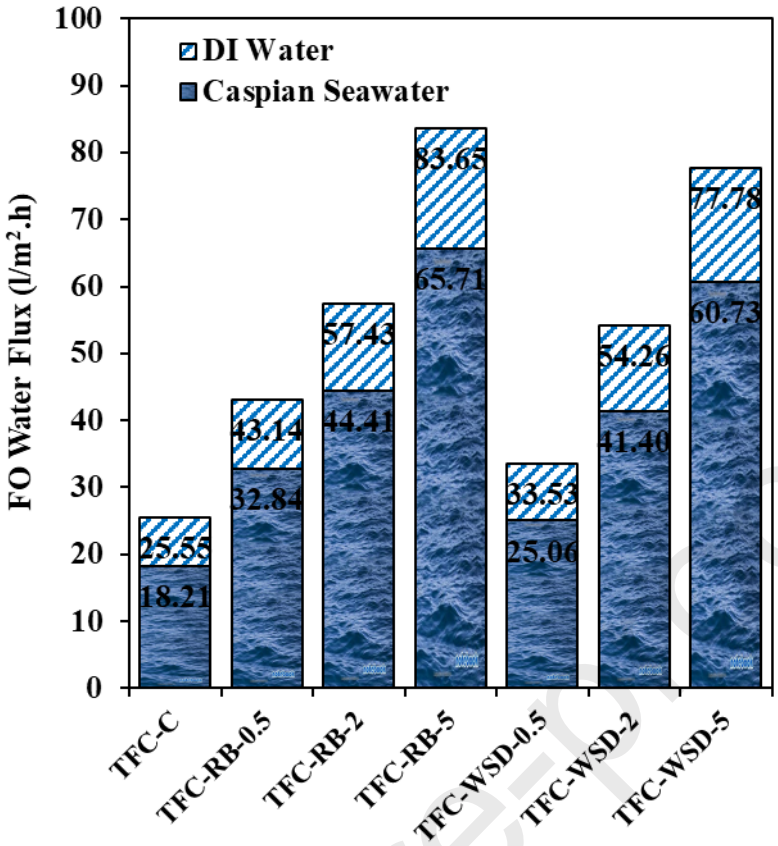

Fig. 16 A comparison between selected TFC FO water flux for DI water, and Caspian seawater as FS, (orientation: FO mode, DS: NaCl 2 M).

Finally, all of the fabricated TFC FO membranes were continuously examined for the desalination of Caspian seawater, and the normalized results of Jw during 30 hours are presented in Fig. 17. As shown in Fig. 17, during the test, the TFC-C membrane showed about 18.48% reduction in Jw. This reduction was attributed to the membrane fouling, attenuation of the osmotic driving force, and DICP phenomenon. The mutation in performance was observed in all fabricated MMM-based TFC FO membranes. According to obtained results, the TFC-WSD-0.5, TFC-RB-0.5, TFC-WSD-2, TFC-RB-2, TFC-WSD-5, and TFC-RB-5, showed about 17, 16.3, 15.4, 14.5, 14, and 12.1% reduction in Jw, respectively. In other words, a sharper drop in Jw was found for the PES-C membrane compared with the fabricated MMM-based TFC FO membranes and the WSD TFC membrane showed a slightly larger drop in the Jw than RB TFC FO membrane.

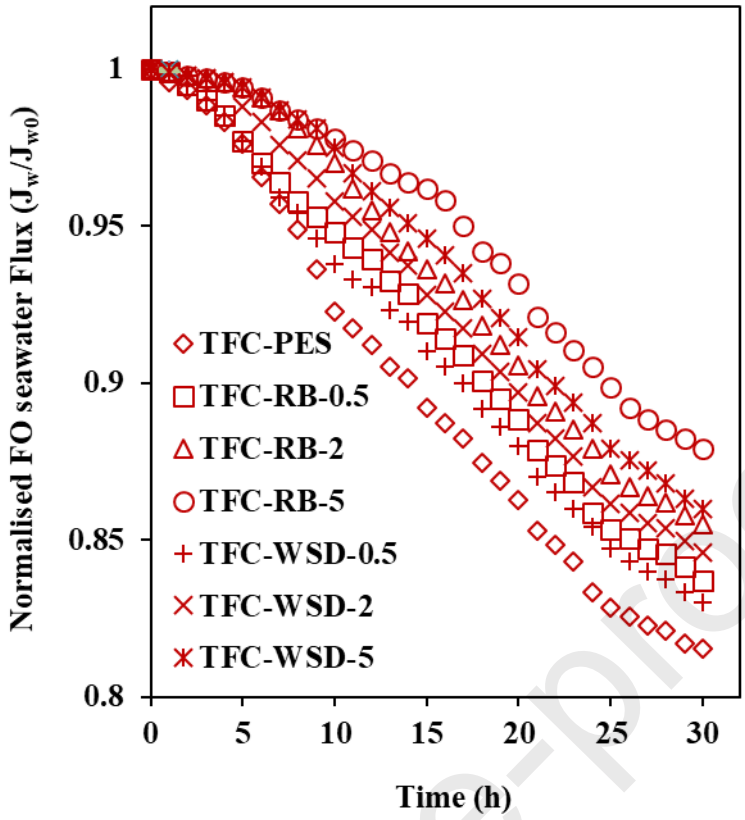

Fig. 17 Normalized selected TFC FO water flux (J_w/J_{w0}) decline over a long time, (orientation: FO mode, FS: Caspian seawater, DS: NaCl 2 M).

4. Conclusions

In this study, PES-based membranes have been successfully modified with the incorporation of natural green raw particles of RB and WSD as porous fillers to fabricate MMM SLs to enhance the water flux (J_w) of TFC FO membranes. Based on FESEM and DLS analyses and with considering the same preparation conditions, RB particles were about four times smaller than WSD particles which also was evident by the results of the water uptake test that showed better results for RB particles. In the case of MMM SLs, by addition of RB and WSD particles into the PES, the diffusion factor ($\varepsilon d_{avg}^2/4t$) was increased in the case of 0.5 wt% of additives and decreased by the further addition of particles (2 & 5 wt%). In the trend of PWP changes, the diffusion factor was the dominant variable because of the minor differences of CAs. Accordingly, the PES-RB-0.5 showed the highest PWP of 160.98 L/m^2.h.bar with the highest

diffusion factor of 5.30. In the case of TFC membranes, some different results, especially in the case of water permeability (A) and FO water flux (J_w), were observed which were justified using the AL cross-linking degree results obtained by the XPS analyses. Due to the insignificant changes of CA and the dominance of the diffusion factor, the cross-linking degree is proportional to the $\varepsilon d_{avg}^2/4t$ factor, which reverses the trend of A-value changes toward PWP. Accordingly, since the diffusion factor of WSD-based membranes is smaller than that of corresponding RB-based membranes, WSD-based membranes showed better results and TFC-WSD-5 showed the highest A-value of 3.31 L/m^2.h.bar with the lowest degree of crosslinking. Also, in the FO experiment with DI water and Caspian seawater as FSs, the RB-based TFC membranes showed better results than WSD-based membranes. The TFC-RB-5 membrane with 2 M NaCl solution as DS exhibited the highest values of J_w of 83.65 and 65.71 L/m^2.h for the DI water and Caspian seawater as FS, respectively. Durability analysis in the period of 30 h for Caspian seawater desalination, also showed the positive impact of using the RB and WSD particles. The importance of these valuable results is that they all achieved at a highly low-cost and in a simple modifying method.

Acknowledgement

The authors acknowledge the funding support of Babol Noshirvani University of Technology through Grant program No. BNUT/389026/99.

Nomenclature and Abbreviations

ICP	internal concentration polarization
FO	forward osmosis
RB	rice bran
WSD	wood sawdust
PES	polyethersulfone
MMM	mixed matrix membrane
SL	support layer
TFC	thin-film composite
FTIR	fourier-transform infrared spectroscopy
FESEM	field emission scanning electron microscope

AFM	atomic force microscopy
XPS	x-ray photoelectron spectroscopy
CA	contact angle
DLS	dynamic light scattering
RO	reverse osmosis
DS	draw solution
AL	active layer
CP	concentration polarization
DICP	dilutive internal concentration polarization
MOF	metal-organic framework
NP	nanoparticle
PA	polyamide
IP	interfacial polymerization
DMF	dimethylformamide
NMP	n-methyl-2-pyrrolidone
TMC	trimesoyl chloride
LiCl	lithium chloride
PVP	polyvinylpyrrolidone
MPD	m-phenylenediamine
DI	deionized water
TDS	total dissolved solids
LN	liquid nitrogen
NIPS	non-solvent-induced phase separation
CECP	concentrative external concentration polarization
PWP	pure water permeation
J_w	FO water flux (L/m^{2}h)
S	structural parameter (μm)
t	Thickness (μm)
τ	tortuosity
ε	Porosity
R	salt rejection
A	water permeability coefficient (L/m^{2}hbar)
B	solute flux (L/m^{2}h)
m_w	weights of the wet samples (mg)
m_d	weights of the dry samples (mg)
J	RO water flux (L/m^{2}h)
ΔP	hydraulic pressure difference (bar)
$\Delta\pi$	osmotic pressure difference (bar)
M	Molarity (mol/L)
ΔV_{feed}	absolute volume change of the FS (L)
Δt	FO test time (h)
π_{DS}	Osmotic pressure of DS (bar)
π_{FS}	Osmotic pressure of FS (bar)
J_s	average reverse salt flux (g/m^{2}h)
C_t	final salt concentrations in the FS (mol/L)
C_0	initial salt concentrations in the FS (mol/L)
A_m	membrane-active area (cm^2)
V_t	final volume of the FS (L)
V_0	initial volume of the FS (L)
D	salt diffusion coefficient (m^2/s)

K	DS resistivity to diffusion (s/μm)
n	relative fractions of the linear part of PA layer
m	relative fractions of the cross-linked part of PA layer
ρ_p	density of polymer (g/cm^3)
ρ_w	density of water (g/cm^3)
m_{wet}	weight of the wet substrates (mg)
m_{dry}	weight of the dry substrates (mg)
d_{avg}	mean pore size (nm)
R_a, R_q	roughness factors (nm)
$\Delta\pi_{eff}$	effective osmotic pressure (bar)

References

1. S. Karmakar, J. Dechnik, C. Janiak, S. De, Aluminium fumarate metal-organic framework: A super adsorbent for fluoride from water, J. Hazard. Mater. 303 (2016) 10-20.

2. A. Criscuoli, A. Figoli, Pressure-driven and thermally-driven membrane operations for the treatment of arsenic-contaminated waters: A comparison, J. Hazard. Mater. 370 (2019) 147-155.

3. J. Hou, P. Liu, M. Jiang, L. Yu, L. Li, Z. Tang, Olefin/paraffin separation through membranes: from mechanisms to critical materials, J. Mater. Chem. A 7 (2019) 23489-23511.

4. Y. Lin, Y. Chen, R. Wang, Thin film nanocomposite hollow fiber membranes incorporated with surface functionalized HKUST-1 for highly-efficient reverses osmosis desalination process, J. Membr. Sci. 589 (2019) 117249.

5. C. H. Park, S. K. Jeon, S.-H. Park, M. G. Shin, M. S. Park, S.-Y. Lee, J.-H. Lee, Cellulose nanocrystal-assembled reverse osmosis membranes with high rejection performance and excellent antifouling, J. Mater. Chem. A 7 (2019) 3992-4001.

6. K. Park, J. Kim, D. R. Yang, S. Hong, Towards a low-energy seawater reverse osmosis desalination plant: A review and theoretical analysis for future directions, J. Membr. Sci. 595 (2020) 117607.

7. B. G. Choi, D. I. Kim, S. Hong, Fouling evaluation and mechanisms in a FO-RO hybrid process for direct potable reuse, J. Membr. Sci. 520 (2016) 89-98.

8. C. F. Wan, T.-S. Chung, Techno-economic evaluation of various RO+PRO and RO+FO integrated processes, Appl. Energ. 212 (2018) 1038-1050.

9. J. Seo, Y. M. Kim, S. H. Chae, S. J. Lim, H. Park, J. H. Kim, An optimization strategy for a forward osmosis-reverse osmosis hybrid process for wastewater reuse and seawater desalination: A modeling study, Desalination 463 (2019) 40-49.

10. J.-Y. Lee, Q. She, F. Huo, C. Y. Tang, Metal–organic framework-based porous matrix membranes for improving mass transfer in forward osmosis membranes, J. Membr. Sci. 492 (2015) 392-399.

11. R, Ramezani Darabi, M. Peyravi, M. Jahanshahi, Modified forward osmosis membranes by two amino-functionalized ZnO nanoparticles: A comparative study, Chem. Eng. Res. Des. 145 (2019) 85-98.

12. M. Qiu, J. Wang, C. He, A stable and hydrophilic substrate for thin-film composite forward osmosis membrane revealed by in-situ cross-linked polymerization, Desalination 433 (2018) 1-9.

13. Y.-N. Wang, K. Goh, X. Li, L. Setiawan, R. Wang, Membranes and processes for forward osmosis-based desalination: Recent advances and future prospects, Desalination 434 (2018) 81-99.

14. X. Wu, M. Shaibani, S. J. D. Smith, K. Konstas, M. R. Hill, H. Wang, K. Zhang, Z. Xie, Microporous carbon from fullerene impregnated porous aromatic frameworks for improving the desalination performance of thin film composite forward osmosis membranes, J. Mater. Chem. A 6 (2018) 11327-11336.

15. R, Ramezani Darabi, M. Jahanshahi, M. Peyravi, A support assisted by photocatalytic Fe_3O_4/ZnO nanocomposite for thin-film forward osmosis membrane, Chem. Eng. Res. Des. 133 (2018) 11-25.

16. X. Zhang, L. Shen, W.-Z. Lang, Y. Wang, Improved performance of thin-film composite membrane with PVDF/PFSA substrate for forward osmosis process, J. Membr. Sci. 535 (2017) 188-199.

17. A. Altaee, A. Sharif, Pressure retarded osmosis: advancement in the process applications for power generation and desalination, Desalination 356 (2015) 31-46.

18. T. Ni, Q. Ge, Highly hydrophilic thin-film composition forward osmosis (FO) membranes functionalized with aniline sulfonate/bisulfonate for desalination, J. Membr. Sci. 564 (2018) 732-741.

19. P. Zhao, B. Gao, Q. Yue, S. Liu, H. K. Shon, The performance of forward osmosis in treating high-salinity wastewater containing heavy metal Ni^{2+}, Chem. Eng. J. 288 (2016) 569-579.

20. Y. Cui, X.-Y. Liu, T.-S. Chung, M. Weber, C. Staudt, C. Maletzko, Removal of organic micro-pollutants (phenol, aniline and nitrobenzene) via forward osmosis (FO) process: Evaluation of FO as an alternative method to reverse osmosis (RO), Water Res. 91 (2016) 104-114.

21. J. R. McCutcheon, M. Elimelech, Influence of concentrative and dilutive internal concentration polarization on flux behavior in forward osmosis, J. Membr. Sci. 284 (2006) 237-247.

22. M. Arjmandi, M. Peyravi, A. Altaee, A. Arjmandi, M. P. Chenar, M. Jahanshahi, E. Binaeian, A state-of-the-art protocol to minimize the internal concentration polarization in forward osmosis membranes, Desalination 480 (2020) 114355.

23. L. Huang, J. R. McCutcheon, Impact of support layer pore size on performance of thin film composite membranes for forward osmosis, J. Membr. Sci. 483 (2015) 25-33.

24. M. Son, H.-g. Choi, L. Liu, E. Celik, H. Park, H. Choi, Efficacy of carbon nanotube positioning in the polyethersulfone support layer on the performance of thin-film composite membrane for desalination, Chem. Eng. J. 266 (2015) 376-384.

25. D. Ma, S. B. Peh, G. Han, S. B. Chen, Thin-Film Nanocomposite (TFN) Membranes Incorporated with Super-Hydrophilic Metal–Organic Framework (MOF) UiO-66: Toward Enhancement of Water Flux and Salt Rejection, ACS Appl. Mater. 9 (2017) 7523-7534.

26. M. Bagherzadeh, A. Bayrami, M. Amini, Enhancing forward osmosis (FO) performance of polyethersulfone/polyamide (PES/PA) thin-film composite membrane via the incorporation of GQDs@UiO-66-NH_2 particles, J. Water Process Eng. 33 (2020) 101107.

27. M. Arjmandi, M. P. Chenar, M. Peyravi, M. Jahanshahi, Physical modification of polymeric support layer for thin film composite forward osmosis membranes by metal–organic framework-based porous matrix membrane strategy, J. Appl. Polym. Sci. 137 (2019) 48672.

28. M. Arjmandi, M. Peyravi, M. P. Chenar, M. Jahanshahi, Channelization of water pathway and encapsulation of DS in the SL of the TFC FO membrane as a novel approach for controlling dilutive internal concentration polarization, Environ. Sci. Water Res. 5 (2019) 1436.

29. M. Arjmandi, M. Peyravi, M. P. Chenar, M. Jahanshahi, A new concept of MOF-based PMM by modification of conventional dense film casting method: Significant impact on the performance of FO process, J. Membr. Sci. 579 (2019) 253-265.

30. R. L. Burritt, C. Herzig, B. D. Tadeo, Environmental management accounting for cleaner production: The case of a Philippine rice mill, J. Clean. Prod. 17 (2009) 431-439.

31. O. Oguntoke, O. K. Otusanya, H. J. Annegarn, Emission of pollutants from wood waste incineration at sawmills in Abeokuta metropolis, Nigeria, Int. J. Environ. Stu. 70 (2013) 964-975.

32. V. Vadivelan, K. V. Kumar, Equilibrium, kinetics, mechanism, and process design for the sorption of methylene blue onto rice husk, J. Colloid Interf. Sci. 286 (2005) 90-100.

33. M. Ghorbani, H. Esfandian, N. Taghipour, R. Katal, Application of polyaniline and polypyrrole composites for paper mill wastewater treatment, Desalination 263 (2010) 279-284.

34. P. Sharma, R. Kaur, C. Baskar, W.-J. Chung, Removal of methylene blue from aqueous waste using rice husk and rice husk ash, Desalination 259 (2010) 249-257.

35. M. Ghorbani, H. Eisazadeh, Removal of COD, color, anions and heavy metals from cotton textile wastewater by using polyaniline and polypyrrole nanocomposites coated on rice husk ash, Compos. B. Eng. 45 (2013) 1-7.

36. T. F Pinto, C. W. B. Bezerra, D. S. A. Silva, E. C. D. S. Filho, A. P. Vieira, C. Airoldi, J. C. P. D. Melo, H. A. S. Silva, S. A. A. Santana, Sawdust Derivative for Environmental Application: Chemistry, Functionalization and Removal of textile dye from aqueous solution, An. Acad. Bras. Cienc. 88 (2016) 1211-1220.

37. S. Larous, A.-H. Meniai, M. B. Lehocine, Experimental study of the removal of copper from aqueous solutions by adsorption using sawdust, Desalination 185 (2005) 483-490.

38. Z. A. Zakaria, M. Suratman, N. Mohammed, W. A. Ahmad, Chromium(VI) removal from aqueous solution by untreated rubber wood sawdust, Desalination 244 (2009) 109-121.

39. M. S. Lashkenari, B. Davodi, H. Eisazadeh, Removal of arsenic from aqueous solution using polyaniline/rice husk nanocomposite, Korean J. Chem. Eng. 28 (2011) 1532-1538.

40. M. Ghorbani, M. S. Lashkenari, H. Eisazadeh, Application of polyaniline nanocomposite coated on rice husk ash for removal of Hg(II) from aqueous media, Synth. Met. 161 (2011) 1430-1433.

41. J. Shah, M. R. Jan, M. Sadia, A.-U. Haq, Preconcentration and determination of Cu (II) from aqueous samples using functionalized sawdust and comparison with synthetic functionalized sorbents, Korean J. Chem. Eng. 30 (2013) 706-713.

42. M. H. Qomi, H. Eisazadeh, M. Hosseini, H. A. Namaghi, Manganese removal from aqueous media using polyaniline nanocomposite coated on wood sawdust, Synth. Met. 194 (2014) 153-159.

43. W. Gan, L. Gao, X. Zhan, J. Li, Removal of Cu^{2+} ions from aqueous solution by amino-functionalized magnetic sawdust composites, Wood Sci. Technol. 51 (2017) 207-225.

44. T. Hou, N. Chen, S. Tong, B. Li, Q. He, C. Feng, Enhancement of rice bran as carbon and microbial sources on the nitrate removal from groundwater, Biochem. Eng. J. 148 (2019) 185-194.

45. S. Bose, C. Das, Preparation and characterization of low-cost tubular ceramic support membranes using sawdust as a pore-former, Mater. Lett. 110 (2013) 152-155.

46. S. Bose, C. Das, Sawdust: From wood waste to pore-former in the fabrication of ceramic membrane, Ceram. Int. 41 (2015) 4070-4079.

47. J. Miao, Y. Yu, Z. Jiang, L. Tang, L. Zhang, Partial delignification of wood and membrane preparation using a quaternary ammonium ionic liquid, Sci. Rep. 7 (2017) 42472.

48. H. A. Namaghi, A. H. Asl, M. P. Chenar, M. Hesampour, A. Pihlajamäki, M. Mänttäri, Performance enhancement of thin-film composite membranes in water desalination process by wood sawdust, Polym. Advan. Technol. 30 (2019) 2802-2818.

49. N. Misdan, W. J. Lau, A. F. Ismail, T. Matsuura, D. Rana, Study on the thin film composite poly(piperazine-amide) nanofiltration membrane: Impacts of physicochemical properties of substrate on interfacial polymerization formation, Desalination 344 (2014) 198-205.

50. J. Wei, C. Qiu, C. Y. Tang, R. Wang, A. G. Fane, Synthesis and characterization of flat-sheet thin film composite forward osmosis membranes, J. Membr. Sci. 372 (2011) 292–302.

51. M. N.-Mahboub, M. Pakizeh, Optimization of preparation conditions of polyamide thin film composite membrane for organic solvent nanofiltration, Korean J. Chem. Eng. 31 (2014) 327-337.

52. B. Khorshidi, T. Thundat, B. A. Fleck, M. Sadrzadeh, Thin film composite polyamide membranes: parametric study on the influence of synthesis conditions, RSC Adv. 5 (2015) 54985-54997.

53. T. Y. Cath, M. Elimelech, J. R. McCutcheon, R. L. McGinnis, A. Achilli, D. Anastasio, A. R. Brady, A. E. Childress, I. V. Farr, N. T. Hancock, J. Lampi, L. D. Nghiem, M. Xie and N. Y. Yip, Standard methodology for evaluating membrane performance in osmotically driven membrane processes, Desalination 312 (2013) 31–38.

54. T. Y. Cath, A. E. Childress and M. Elimelech, Forward osmosis: Principles, applications, and recent developments, J. Membr. Sci. 281 (2006) 70-87.

55. S. Chou, L. Shi, R. Wang, C. Y. Tang, C. Qiu and A. G. Fane, Characteristics and potential applications of a novel forward osmosis hollow fiber membrane, Desalination 261 (2010) 365-372.

56. O. Akin and F. Temelli, Probing the hydrophobicity of commercial reverse osmosis membranes produced by interfacial polymerization using contact angle, XPS, FTIR, FE-SEM and AFM, Desalination 278 (2011) 387-396.

57. M. Arjmandi, O. Pirouzram and A. Ahmadpour, A new approach for determination of neck-pore size distribution of porous membranes via bubble point data, Int. J. Eng. Trans. C 28 (2015) 823-831.

58. A. Shahsavand and M. N. Shahrak, Direct pore size distribution estimation of heterogeneous nano-structured solid adsorbents from condensation data: Condensation with no prior adsorption, Colloids Surf. A 378 (2011) 1–13.

59. P. Sukitpaneenit and T. S. Chung, Molecular elucidation of morphology and mechanical properties of PVDF hollow fiber membranes from aspects of phase inversion, crystallization and rheology, J. Membr. Sci. 340 (2009) 192–205.

60. W. Gan, L. Gao, X. Zhan, J. Li, Removal of Cu^{2+} ions from aqueous solution by amino-functionalized magnetic sawdust composites, Wood Sci. Technol. 51 (2017) 207-225.

61. G. Wolansky, A. Marmur, Apparent contact angles on rough surfaces: the Wenzel equation revisited, Colloid. Surface. A 156 (1999) 381-388.

62. G. D. Vilakati, E. M. V. Hoek, B. B. Mamba, Probing the mechanical and thermal properties of polysulfone membranes modified with synthetic and natural polymer additives, Polym. Test. 34 (2014) 202-210.

63. C. Y. Tang, Y.-N. Kwon, J. O. Leckie, Probing the nano- and micro-scales of reverse osmosis membranes-A comprehensive characterization of physiochemical properties of uncoated and coated membranes by XPS, TEM, ATR-FTIR, and streaming potential measurements, J. Membr. Sci. 287 (2007) 146-156.

Research highlights

- TFC membranes supported on RB- and WSD-based MMMs were fabricated for FO process
- Incorporation of both RB and WSD particles in the TFC SL resulted in a dramatic decrease in structural parameters
- Control of the DICP phenomenon was achieved with the use of RB and WSD particles
- The positive impact of using the RB and WSD particles on Caspian seawater desalination was evident
- These valuable results achieved at a highly low-cost and in a simple modifying method

Declaration of interests

☒ The authors declare that they have no known competing financial interests or personal relationships that could have appeared to influence the work reported in this paper.

☐The authors declare the following financial interests/personal relationships which may be considered as potential competing interests: